

Fast Low Rank column-wise Compressive Sensing for Accelerated Dynamic MRI

Silpa Babu*, Sajan Goud Lingala**, Namrata Vaswani*

*ECE dept, Iowa State University, USA

**BME dept, University of Iowa, USA

Abstract—This work develops a fast, memory-efficient, and ‘general’ algorithm for accelerated/undersampled dynamic MRI by assuming an approximate LR model on the matrix formed by the vectorized images of the sequence. By ‘general’, we mean that our algorithm can be used for multiple accelerated dynamic MRI applications and multiple sampling rates (acceleration rates) and patterns with a single choice of parameters (no parameter tuning). We show that our proposed algorithms, alternating Gradient Descent (GD) and minimization for MRI (altGDmin-MRI and altGDmin-MRI2), outperform many existing approaches while also being faster than all of them, on average. This claim is based on comparisons on 8 different retrospectively undersampled single- or multi-coil dynamic MRI applications, undersampled using either 1D Cartesian or 2D pseudo-radial undersampling at multiple sampling rates. All comparisons used the same set of algorithm parameters. Our second contribution is a mini-batch and a fully online extension that can process new measurements and return reconstructions either as soon as measurements of a new image frame arrive, or after a short delay.

I. INTRODUCTION

Dynamic Magnetic Resonance Imaging (MRI) is a powerful imaging modality to non-invasively capture time evolving phenomena in the human body, such as the beating heart, motion of vocal tract during speaking, or dynamics of contrast uptake in brain. A long standing challenge in MRI is its slow imaging speed which restricts its full potential in the achievable spatial or temporal resolution. From a signal processing standpoint, in MRI, one measures the 2D discrete Fourier transform (FT) of a slice of the organ being imaged, one FT coefficient (or one line of coefficients) at a time. This makes the imaging slow. Accelerated/undersampled/compressive dynamic imaging involves the design of algorithms to accurately reconstruct the image sequence from undersampled Fourier domain data (referred to as k-space data in MRI literature). Accelerated MRI is, in fact, one of the key practical applications where Compressive Sensing (CS) ideas have been used. This includes both work that uses traditional (sparse) CS [1], [2] for single image MRI, as well as later work that relies on structured sparsity or low-rank (LR) assumptions, e.g., [3], [4], [5], [6].

A. Our Contributions

This work develops a fast, memory-efficient, and ‘general’ algorithm for accelerated dynamic MRI by assuming an approximate LR model on the matrix formed by the vectorized images of the sequence. In analogy with traditional (sparse) CS, we refer to the problem of reconstruction with this

modeling assumption as LR column-wise CS (LRcCS). By ‘general’, we mean that our algorithm can be used for multiple accelerated dynamic MRI applications and multiple sampling rates (acceleration rates) or sampling patterns (pseudo-radial or 1D Cartesian or true radial) with a single choice of parameters (no parameter tuning). Via extensive experiments on 8 different retrospectively undersampled single-coil or multi-coil dynamic MRI applications, undersampled using 1D Cartesian or pseudo-radial undersampling¹ with 16, 8, or 4 radial lines, we show that, on average, our proposed algorithms, alternating Gradient Descent (GD) and minimization for MRI (altGDmin-MRI and altGDmin-MRI2), outperforms many existing approaches while also being faster than all of them – the two existing LRcCS algorithms that come with theoretical guarantees for Gaussian measurements; three LRcCS approaches from dynamic MRI literature; and one deep learning (DL) based approach trained on static images. All experiments are done with a fixed set of parameters.

AltGDmin-MRI is a modification of altGDmin which is a fast GD-based algorithm that was developed in our recent work [10] to provably solve the LRcCS problem. Since we represent the matrix formed by the unknown image sequence as $\mathbf{X} = \mathbf{U}\mathbf{B}$ where \mathbf{U} and \mathbf{B} are matrices with r columns and rows respectively, with r being the assumed (low) rank, storing and processing \mathbf{U}, \mathbf{B} requires memory of size only $\max(n, q)r$ instead of nq . This means that a memory-efficient implementation of our approach can be developed for settings where n (image size) or q (sequence length) are very large.

We also develop mini-batch and fully online (initialized with a mini-batch) extensions of altGDmin-MRI that can process new measurements and return reconstructions after a much shorter data acquisition delay than the full batch solution. The fast, and even more memory-efficient, reconstructions enabled by these schemes have the potential to advance real-time vocal tract shaping experiments during speaking. For example, it is common practice to use a quick yet suboptimal reconstruction for several tasks that need quick feedback, e.g., on the fly adjustment of the center frequency when using spiral readouts, to minimize blur at the air-tissue boundaries, or on the fly adjustment of scan planes when the subject is producing sounds of interest. Certain speech sounds are captured well in oblique planes, and warrant almost real-time inspection.

¹As we explain in Sec. VI, it is well understood that pseudo-radial undersampling results in negligible loss in image quality while allowing for much faster reconstruction algorithms; in fact for CS methods, there is also sometimes an improvement in reconstruction quality [7], [8], [9].

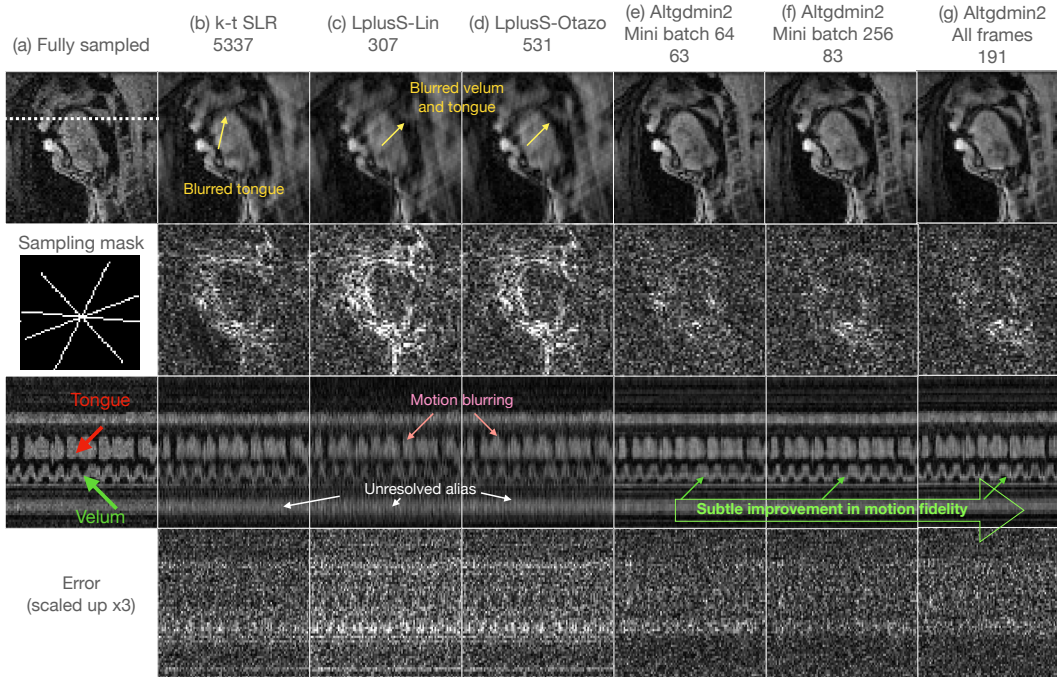


Fig. 1: Comparisons of reconstruction algorithms on long speech MRI sequence using 4 radial lines/frame. In the second row, we show the image time profile. This is cut through the tongue and velum depicting the motion of these articulators. Only 100 out of 2048 image frames are shown for the sake of brevity. Error images are calculated as difference between fully sampled and reconstructed images. Observe that ktSLR, L+S-Lin, and L+S-Otazo reconstructions have motion blurring and/or alias artifacts. In contrast, altGDmin-MRI2 (altgadmin2) reconstructions even with smaller batch sizes produce superior reconstructions. As expected, smaller batch sizes produce faster reconstructions. With larger batch sizes, the temporal sharpness (or motion fidelity) improve but only subtly.

B. Existing work

Provable solutions with only simulation experiments. There are two other existing provable solutions to the LRcCS problem. The first is an Alternating Minimization (AltMin) solution that is designed to solve a generalization of LRcCS [11], [12] and hence also solves LRcCS. The second studies a convex relaxation called mixed norm minimization [13]. The third is the altGDmin solution [10] that we modify in the current work. The convex solution is extremely slow, both theoretically and experimentally. The AltMin solution is faster than the convex one, but still significantly slower than altGDmin [10]. The numerical experiments provided in all these works only use simulated LR matrices and simulated Gaussian measurements. *MRI literature: LR or sparse model approaches.* Since the work on CS in the early 2000s there has been extensive work on exploiting sparsity of the image or of the sequence in different dictionaries and bases in order to enable accelerated MRI, e.g., see [1], [14] and follow-up work. For settings where joint reconstruction of a set of similar images is needed, a low rank (LR) assumption on the matrix formed by arranging the images as its columns is a more flexible model since it does not require knowledge of the sparsifying basis or dictionary. MR images change slowly over time and hence are well-modeled as being approximately LR. Prior LRcCS model based solutions to undersampled dynamic MRI [15], [3], [16], [4], [17], [5], [6] can be classified into three broad categories: (a) methods which enforce the LR constraint in an explicit manner, e.g., via explicit estimation of the temporal subspace from low spatial, but high temporal resolution, training data [3], [16], [17], (b) follow-up works in which improved self

navigated Partially Separable Function (PSF) models were proposed [18], [19], and (c) methods that enforce the LR constraint in an implicit manner, e.g., via the nuclear norm or Schatten- p norm regularization with $p < 1$ as in k-t-SLR [4] and follow-up work [5], [6]. Some of these, such as k-t-SLR, assume both total variation norm sparsity of each image, and the LR model on the sequence. Methods of type (b) and (c) do not require training data and hence offer more flexibility in handling arbitrary sampling patterns.

A related line of work, inspired by the robust PCA literature [20], models the matrix formed by the MRI sequence as being LR plus sparse (L+S). These methods decompose the dynamic time series as a sum of a LR component modeling smoothly varying time series (e.g. object background, and/or smooth contrast changes as in perfusion MRI), and a sparse component which models the other changes in the image; see [21] (L+S-Otazo), [22] (L+S-Lin), and follow-up works, e.g. [23], [?].

An important challenge with k-t-SLR, L+S-Otazo, L+S-Lin, and most follow-up work, is the need for carefully tuning the parameters (regularization parameters and other hyperparameters associated with the iterative optimization algorithm) for different dynamic MRI applications. Most published work provides results and code/parameters that work well for only the chosen application. A second limitation of the iterative optimization algorithms developed in the above works is that they are slow when used for large matrix dimensions.

Motion often breaks down the assumption of low rank in dynamic MRI. There has been extensive work on motion estimation and compensation before imposing the structural assumptions [24], [25], [26], [14]. While these approaches

handle motion better, these schemes have even more parameters and each MRI application needs very specific parameter tuning. Also, these are even slower.

Reconstruction algorithm speed is a very important concern in applications needing low latency such as real-time interactive MRI, interventional MRI, or biofeedback imaging. However, even in other situations, if a reconstruction can be obtained without making the patient wait too long or return later, it would considerably improve clinical workflow and overall throughput. Immediate reconstructions can also allow for on the fly identification of certain artifacts, which can be immediately corrected (e.g., adjusting center frequency to minimize off-resonance artifacts, rescanning if subject experiences sudden motion such as cough, etc). Fast reconstructions therefore reduces unnecessary overhead cost associated with re-scheduling patient scans.

MRI literature: Deep Learning (DL) methods. There has been much recent work on use of various DL techniques in the MRI literature. The most common set of DL-based approaches are supervised DL reconstruction schemes, e.g., [27], [28], [29], [30], [31]. These need a large numbers of fully sampled training data points. While such data can be acquired in static imaging applications (e.g., by extending scan times from cooperative volunteers, or compliant patients), it is not straightforward to acquire sufficient number of fully sampled image sequences for dynamic imaging applications, and definitely not for high time resolution applications, which warrants need of highly under-sampled acquisitions in the first place. For this reason, a majority of supervised DL models have been used to perform reconstruction frame by frame in dynamic MRI. This approach has three problems: (i) It does not fully exploit redundancies along the temporal dimension and hence does not always outperform sparsity or LR based methods. We demonstrate this via comparison with the approach of [29] in Sec. VI. (ii) DL model learning/training can be very computationally, and hence energy-wise, expensive. The reason is training with one set of parameters may not yield the best results and hence the parameters need to be tuned. Each tuning requires re-training. (iii) The parameters are learned for one specific MRI application, and the same network does not give good results for another application.

Good quality (motion-free) training sequences can be acquired in situations where the motion may be freed, e.g., in breath held segmented cardiac cine MRI by breathholding, and ECG gating. For such settings, researchers have proposed supervised DL models that exploit spatio-temporal redundancies [32], [33], [34], [35]. For this class of approaches, besides training time, memory requirement is another big constraint. Limited memory on GPUs makes it hard to generalize these approaches to high dimensional dynamic MRI applications such as 4D (x,y,z + time) or 5D (x,y,z,flow+time).

In very recent literature, unsupervised DL based dynamic MRI methods have been proposed. These models exploit spatio-temporal redundancies in the dataset without the use of fully sampled reference datasets [36], [37]. These approaches have so far only been developed, and results demonstrated, for real-time free breathing cardiac MRI datasets. Their two important limitations are the algorithm speed and the memory

requirement. Since these approaches do not use a pre-trained network, but instead train the deep network on the test/query data, the recovery time needed is very large. As an example, to reconstruct a typical speech sequence with $n = 100^2 = 10000$ pixels and $q = 500$ frames, this class of approaches needs 45mins to an hour on a GPU. Our algorithm only needs 1-2 minutes for a similar dataset.

Our approach. In contrast to above methods, our approach is fast, memory-efficient, and exploits spatial and temporal redundancies in the dataset, without needing any training data (or the expensive training phase that most DL methods need). Moreover, it needs only a few parameters to be set and these do not need application-specific tuning.

Other related work on online or mini-batch algorithms. Other somewhat related work from the compressive sensing MRI literature that also develops online or minibatch algorithms includes [38], [39], and follow-up methods.

C. Paper Organization

We provide the notation, the LRcCS problem setting and the one assumption it needs (repeated from [10]), and the 3-level approximate-LRcCS model in Sec. II. We explain the basic altGDmin algorithm idea [10], followed by explaining our approach for automated parameter setting in Sec. III. The modifications for approximate-LRcCS are developed in Sec. IV. Mini-batch and online subspace tracking methods are proposed in Sec. V. Detailed experimental evaluations and comparisons are provided in Sec. VI. We conclude in Sec. VII.

II. PROBLEM SETTING

A. Notation

Everywhere, $\|\cdot\|_F$ denotes the Frobenius norm, $\|\cdot\|$ without a subscript denotes the (induced) l_2 norm, $^\top$ denotes (conjugate) transpose, and $M^\dagger := (M^\top M)^{-1}M^\top$. For a vector w , $|w|$ computes the magnitude of each on entry of w . For a scalar α , $\mathbb{1}(w \leq \alpha)$ returns a vector of 1s and 0s of the same size as w with 1s where $w(k) \leq \alpha$ and zero everywhere else. Here $w(k)$ is the k -th entry of w . We use \circ to denote the Hadamard product. Thus $z := w \circ \mathbb{1}(|w| \leq \alpha)$ zeroes out entries of w with magnitude larger than α .

B. Basic LRcCS for dynamic MRI and the assumption needed

We would like to recover an $n \times q$ rank- r matrix $X^* = [x_1^*, x_2^*, \dots, x_q^*]$, with $r \ll \min(q, n)$, from

$$y_k = A_k x_k^*, \quad k \in [q] \quad (1)$$

when y_k is an m_k -length vector with $m_k < n$, and the measurement matrix A_k is $m_k \times n$. For dynamic MRI, x_k^* is the k -th vectorized image and, so, the matrix X^* corresponds to the (unknown) image sequence that needs to be reconstructed. Each image has n pixels and there are q images in the sequence. The measurement matrices A_k are partial Fourier (applied on different weighted versions of x_k^*), with $m_k \ll n$. We define these matrices in Sec. II-D below.

We let $X^* \stackrel{\text{SVD}}{=} U^* \Sigma^* V^*$ denote its reduced (rank r) SVD, and $\kappa := \sigma_{\max}^*/\sigma_{\min}^*$ the condition number of Σ^* . We let $B^* := \Sigma^* V^*$, so that $X^* = U^* B^*$. Their k -th columns are denoted by x_k^* , b_k^* respectively.

Let $m = \max(m_k)$. We define the $m \times n$ matrix $Y = [(y_1)_{\text{InG}}, (y_2)_{\text{InG}}, \dots, (y_q)_{\text{InG}}]$ with $(y_k)_{\text{InG}}$ being the vector

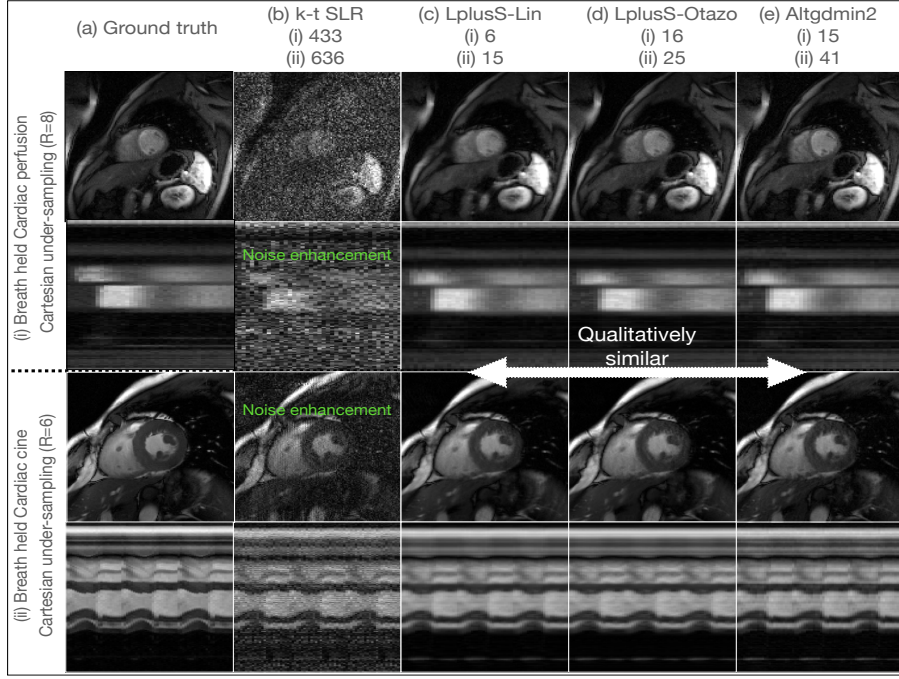


Fig. 2: Qualitative comparison of reconstruction algorithms on Cartesian undersampled breath held cardiac perfusion and cardiac cine datasets, previously used in [21], [22]. 1D undersampling mask used are shown. A spatial frame along with the image time series along the horizontal white dotted line are shown. In the cardiac cine dataset, the images were repeated by a factor of 3 along the time dimension to better visualize the motion dynamics. We observe k-t SLR to have considerable noise enhancement in both the datasets. The proposed AltGDmin2-MRI algorithm provides qualitatively similar results to the L+S-Lin and L+S-Otazo algorithms.

\mathbf{y}_k followed by $(m - m_k)$ zeros. Similarly let $(\mathbf{A}_k)_{\text{lng}}$ be an $m \times n$ matrix with $(m - m_k)$ rows of zeros at the end. Then, (1) can also be written as a linear operator applied to the entire matrix \mathbf{X}^* as

$$\mathbf{Y} = \mathcal{A}(\mathbf{X}^*) := [(\mathbf{A}_1)_{\text{lng}}(\mathbf{x}_1^*), (\mathbf{A}_2)_{\text{lng}}(\mathbf{x}_2^*), \dots, (\mathbf{A}_q)_{\text{lng}}(\mathbf{x}_q^*)] \quad (2)$$

Similarly $\mathcal{A}^\top(\mathbf{Y})$ returns the $n \times q$ matrix with columns $(\mathbf{A}_k)_{\text{lng}}^\top(\mathbf{y}_k)_{\text{lng}}$, i.e. $\mathcal{A}^\top(\mathbf{Y}) = [(\mathbf{A}_1)_{\text{lng}}^\top(\mathbf{y}_1)_{\text{lng}}, (\mathbf{A}_2)_{\text{lng}}^\top(\mathbf{y}_2)_{\text{lng}}, \dots, (\mathbf{A}_q)_{\text{lng}}^\top(\mathbf{y}_q)_{\text{lng}}]$.

Assumption. Another way to understand our problem is as follows: each scalar measurement \mathbf{y}_{ki} (i -th entry of \mathbf{y}_k) satisfies $\mathbf{y}_{ki} := \langle \mathbf{a}_{ki}, \mathbf{x}_k^* \rangle$, $i \in [m]$, $k \in [q]$ with \mathbf{a}_{ki}^\top being the i -th row of \mathbf{A}_k . Observe that the measurements are not global, i.e., no \mathbf{y}_{ki} is a function of the entire matrix \mathbf{X}^* . The measurements are global for each column but not across the different columns. We thus need the following incoherence assumption to enable correct interpolation across the different columns [11]. This was introduced in [40] for LR matrix completion (LRMC) which is another LR problem with non-global measurements.

Assumption 2.1 (Right singular vectors' incoherence). *We assume that $\max_k \|\mathbf{b}_k^*\| \leq \mu \sigma_{\max} \sqrt{r/q}$. Treating κ as a constant, up to constants, this is equivalent to requiring that $\max_k \|\mathbf{x}_k^*\|^2 \leq \kappa^2 \mu^2 \sum_{k=1}^q \|\mathbf{x}_k^*\|^2 / q$ [10].*

This assumption assumes that the “energy” (squared 2-norm) of the different columns \mathbf{x}_k^* (different images in the sequence) is similar so that so that the maximum energy is within a constant factor of its average value. This is valid

for medical image sequences for which large energy changes across the sequence cannot happen.

C. Approximate-LRcCS for dynamic MRI

Most MRI sequences have a certain baseline component that is roughly constant across the entire sequence. We refer to this as the “mean” image, $\bar{\mathbf{z}}^*$. It can be verified experimentally that the norm of this mean is large compared to that of any of the columns of the matrix formed by subtracting it out. Secondly, MR image sequences, and in fact, most real image sequences, are only approximately LR, i.e., the residual after subtracting the LR component is not zero, but has a small magnitude.

Thus the following 3-level model is a more appropriate model for dynamic MRI. Let \mathbf{z}_k^* be the vectorized k -th MR image. Then, we are assuming that

$$\mathbf{z}_k^* = \bar{\mathbf{z}}^* + \mathbf{x}_k^* + \mathbf{e}_k^*, \quad \text{for all } k \in [q],$$

with $\|\mathbf{e}_k^*\| \ll \|\mathbf{x}_k^*\| \ll \|\bar{\mathbf{z}}^*\|$. Here $\bar{\mathbf{z}}^*$ is the vectorized “mean” image, the \mathbf{x}_k^* 's form a rank r matrix \mathbf{X}^* , and \mathbf{e}_k^* is the unstructured residual signal component, which we refer to as the modeling error. We consider two models on \mathbf{e}_k^* . The first does not assume any structure on \mathbf{e}_k^* 's. The second assumes temporal Fourier sparsity, i.e., that the rows of the matrix \mathbf{E}^* are Fourier sparse.

We develop a 3-level hierarchical algorithm that first recovers $\bar{\mathbf{z}}^*$, then \mathbf{x}_k^* 's, then \mathbf{e}_k^* 's. From the perspective of minimizing the reconstruction error for most sequences, it is only marginally useful to try to recover \mathbf{e}_k^* 's. See Table I, columns 4 and 5. However, recovering it significantly helps visual image quality. More importantly, it is needed to reconstruct and detect

abnormalities in organ functions which may appear only in few images of few sequences out of the many that are imaged.

D. Single- and Multi-coil MRI models

In case of single-coil dynamic MRI, $\mathbf{A}_k = \mathbf{H}_k \mathbf{F}$ where \mathbf{F} is an $n \times n$ matrix that models computing the 2D discrete Fourier Transform (DFT) of the vectorized image as a matrix-vector product. The matrix \mathbf{H}_k is a ‘‘mask matrix’’ of size $m_k \times n$ with entries being either one or zero. It contains exactly one 1 in each row (corresponding to the observed DFT frequency converted to 1D coordinates). The mask matrix \mathbf{H}_k is decided by the specific random sampling trajectory (specified in Sec. VI).

In case of multi-coil MRI with mc coils, there are mc MR scanners with each of them capturing a subset of Fourier coefficients of a differently weighted version of the cross-section to be imaged. In matrix-vector notation, the measurement model is as follows.

$$\mathbf{y}_k = \begin{bmatrix} \mathbf{y}_{k,1} \\ \mathbf{y}_{k,2} \\ \vdots \\ \mathbf{y}_{k,mc} \end{bmatrix} = \underbrace{\begin{bmatrix} \mathbf{M}_k \mathbf{F} \mathbf{D}_1 \\ \mathbf{M}_k \mathbf{F} \mathbf{D}_2 \\ \vdots \\ \mathbf{M}_k \mathbf{F} \mathbf{D}_{mc} \end{bmatrix}}_{\mathbf{A}_k} \mathbf{x}_k^*$$

where $\mathbf{D}_j = \text{diag}(\mathbf{d}_j)$ are $n \times n$ diagonal matrices with diagonal entries (entries of the vector \mathbf{d}_j) being the coil sensitivities of the j -th coil. We should point out that $\mathbf{D}_j \mathbf{x} = \mathbf{d}_j .* \mathbf{x}$ where $*$ is MATLAB notation for Hadamard product, thus $\mathbf{D}_j \mathbf{x}$ is equivalent to weighting the l -th pixel \mathbf{x}_l by $(\mathbf{d}_j)_l$. Each $\mathbf{y}_{k,j}$ is an m_k length vector and thus \mathbf{y}_k is of length $m_k \cdot mc$.

III. SOLVING BASIC LRCCS FOR EXACT AND

APPROXIMATE LR MATRICES

A. Alternating GD with Minimization (altGDmin) algorithm

To understand the basic idea, assume here that \mathbf{X}^* is an exactly LR matrix with rank r and r is known.

We would like to design a GD based solution to find the matrix \mathbf{X} that minimizes the squared loss cost function $\tilde{f}(\mathbf{X}) := \sum_{k=1}^q \|\mathbf{y}_k - \mathbf{A}_k \mathbf{x}_k\|^2$ subject to the constraint that its rank is r or less. There are two commonly used GD approaches in the LR recovery literature, and in particular for LRMC. The first is to use projected GD on \mathbf{X} : at each iteration, perform one step of GD w.r.t. \mathbf{X} , followed by projecting the resulting matrix onto the space of rank r matrices (by SVD) [41]. The second is to write $\mathbf{X} = \mathbf{U}\mathbf{B}$ where \mathbf{U} is $n \times r$ and \mathbf{B} is $r \times q$ and do alternating GD on \mathbf{U} and \mathbf{B} for a cost function that contains the data term, $f(\mathbf{U}\mathbf{B})$, plus a term that helps ensure that norms of \mathbf{U} and \mathbf{B} remain similar [42], [43]. This norm-balancing term is critical because, without it, alternating GD can result in the norm of one of \mathbf{U} or \mathbf{B} increasing in an unbounded fashion while that of the other decreases to zero and this creates numerical problems. However, as explained in [10], due to the specific asymmetric measurement model of LRcCS, it is not possible to prove that either of the above approaches works (error decays to a small enough value)².

²Briefly, the reason is that, in both cases, the estimates of the different columns are coupled (estimate $\hat{\mathbf{x}}_k$ or $\hat{\mathbf{b}}_k$ depends on all columns of \mathbf{X}^*). This means that it is not possible to get a tight bound on the column-wise (image-wise) error, $\max_k (\|\hat{\mathbf{x}}_k - \mathbf{x}_k^*\| / \|\mathbf{x}_k^*\|)$. But this is needed in order to bound the gradient norm with high probability under the desired sample complexity.

Moreover, even for LRMC where these approaches do work, the first approach is memory-intensive (the gradient w.r.t. \mathbf{X} is an $n \times q$ matrix that is not LR); while the second one is slow: it needs a GD step size that is $1/r$ or smaller [42], [43], making it r -times slower than GD with a constant step size.

The following modification of alternating GD, that we dub *altGDmin*, is as fast as projected GD on \mathbf{X} , is as memory-efficient as altGD, and its estimates $\hat{\mathbf{b}}_k$ are uncoupled (making it possible to get the desired column-wise error bound) [10]. Let $\mathbf{X} = \mathbf{U}\mathbf{B}$ and consider

$$f(\mathbf{U}, \mathbf{B}) := \tilde{f}(\mathbf{U}\mathbf{B}) = \sum_{k=1}^q \|\mathbf{y}_k - \mathbf{A}_k \mathbf{U} \mathbf{b}_k\|^2.$$

altGDmin involves iterating over the following two steps.

- 1) We use projected GD for updating \mathbf{U} : one GD step w.r.t. \mathbf{U} followed by projecting onto the space of orthonormal matrices (by using QR decomposition).
- 2) For each new estimate of \mathbf{U} , we solve for \mathbf{B} by minimizing over it while keeping \mathbf{U} fixed at its current value. Because our measurements are column-wise decoupled, the minimization step gets decoupled for the different columns of \mathbf{B} , i.e.,

$$\min_{\mathbf{B}} f(\mathbf{U}, \mathbf{B}) = \sum_{k=1}^q \min_{\mathbf{b}_k} \|\mathbf{y}_k - \mathbf{A}_k \mathbf{U} \mathbf{b}_k\|^2.$$

This problem is now a column-wise least squares (LS) problem with \mathbf{b}_k being an r -length vector and $\mathbf{A}_k \mathbf{U}$ being $m_k \times r$ matrix. Thus, the complexity per column is only $m_k r^2$ (solving LS) plus $m_k n r$ (cost of computing $\mathbf{A}_k \mathbf{U}$). Thus the total cost of the LS step is $O((m_k r^2 + m_k n r) q) = O(m n r q)$ which is equal to the cost of one GD step for \mathbf{U} .

Finally, since $f(\mathbf{U}, \mathbf{B})$ is not convex in the unknowns $\{\mathbf{U}, \mathbf{B}\}$, the above algorithm needs a careful initialization of one of them (zero initialization will not always work). First, suppose that $m_k = m_1 = m$. We obtain an initial estimate of \mathbf{U} by computing the top r left singular vectors of the matrix

$$\mathbf{X}_0 := \begin{bmatrix} \frac{1}{m} (\mathbf{A}_1^\top \mathbf{y}_{1, \text{trunc}}(\alpha)), \dots, \frac{1}{m} (\mathbf{A}_k^\top \mathbf{y}_{k, \text{trunc}}(\alpha)), \\ \dots, \frac{1}{m} (\mathbf{A}_q^\top \mathbf{y}_{q, \text{trunc}}(\alpha)) \end{bmatrix} \quad (3)$$

where $\alpha := \tilde{C} \frac{\sum_{ki} (\mathbf{y}_{ki})^2}{mq}$ and $\mathbf{y}_{k, \text{trunc}}(\alpha) := \mathbf{y}_k \circ \mathbb{1}(|\mathbf{y}_k| \leq \sqrt{\alpha})$ [10]. To understand the above idea, observe that \mathbf{X}_0 is a truncated version of $\mathbf{X}_{0, \text{full}}$ which is the above matrix with $\mathbf{y}_{k, \text{trunc}}(\alpha)$ replaced by \mathbf{y}_k . If \mathbf{A}_k contains i.i.d. standard Gaussian entries, it is easy to see that $\mathbb{E}[\mathbf{X}_{0, \text{full}}] = \mathbf{X}^*$. The truncation zeroes out entries \mathbf{y}_{ki} whose squares are large compared to their empirical mean, $\frac{\sum_{ki} (\mathbf{y}_{ki})^2}{mq}$. This makes the summands of \mathbf{X}_0 lighter tailed, so that the required concentration around \mathbf{X}^* holds w.h.p. [10].

We summarize the complete algorithm that is used in all our experiments in Algorithm 1. This includes the automatic parameter setting explained in Sec. III-B below. We state the theoretical guarantee for it (for the random Gaussian \mathbf{A}_K setting) from [10] in Appendix B provided in the Supplement.

Algorithm 1 *auto-altGDmin: altGDmin with automated parameter setting.* Let $M^\dagger := (M^\top M)^{-1} M^\top$.

- 1: **Input:** $\mathbf{y}_k, \mathbf{A}_k, k \in [q]$.
- 2: **Parameter setting is specified in blue.**
- 3: **Initialization:**
- 4: **Set $\tilde{C} = 36$**
- 5: Compute $\alpha = \tilde{C} \frac{1}{m_q} \sum_{ki} |\mathbf{y}_{ki}|^2$, $\mathbf{y}_{k, trunc} = \mathbf{y}_k \circ \mathbb{1}\{|\mathbf{y}_k| \leq \sqrt{\alpha}\}$, $\bar{m} = \sum_{k=1}^q m_k/q$, and compute

$$\mathbf{X}_0 := \left[\frac{1}{\sqrt{m_1 \bar{m}}} (\mathbf{A}_1^\top \mathbf{y}_{1, trunc}), \dots, \frac{1}{\sqrt{m_k \bar{m}}} (\mathbf{A}_k^\top \mathbf{y}_{k, trunc}), \dots, \frac{1}{\sqrt{m_q \bar{m}}} (\mathbf{A}_q^\top \mathbf{y}_{q, trunc}) \right]$$

- 6: Let $\sigma_j = \sigma_j(\mathbf{X}_0)$. Set \hat{r} as the smallest integer for which

$$\sum_{j=1}^r \sigma_j^2 \geq (b/100) \cdot \sum_{j=1}^{\min(n,q,m)/10} \sigma_j^2, \quad b = 85$$

- 7: Set $\hat{\mathbf{U}}_0 \leftarrow$ top \hat{r} left singular vectors of \mathbf{X}_0
- 8: **GDmin iterations: Set $T_{max} = 70$**
- 9: **for** $t = 1$ **to** T_{max} **do**
- 10: Let $\hat{\mathbf{U}} \leftarrow \hat{\mathbf{U}}_{t-1}$.
- 11: Update $\hat{\mathbf{B}}$: For all $k \in [q]$, $\hat{\mathbf{b}}_k \leftarrow (\mathbf{A}_k \hat{\mathbf{U}})^\dagger \mathbf{y}_k$.
- 12: Update $\hat{\mathbf{X}}$: For all $k \in [q]$, $\hat{\mathbf{x}}_k \leftarrow \hat{\mathbf{U}} \hat{\mathbf{b}}_k$
- 13: Gradient compute:

$$\nabla_U f(\hat{\mathbf{U}}, \hat{\mathbf{B}}) \leftarrow \sum_{k=1}^q \mathbf{A}_k^\top (\mathbf{A}_k \hat{\mathbf{U}} \hat{\mathbf{b}}_k - \mathbf{y}_k) \hat{\mathbf{b}}_k^\top$$

- 14: **If** $t = 1$, **set** $\eta = 0.14/\|\nabla_U f(\hat{\mathbf{U}}, \hat{\mathbf{B}})\|$.
- 15: GD step for $\hat{\mathbf{U}}$: $\hat{\mathbf{U}}^+ \leftarrow \hat{\mathbf{U}} - \eta \nabla_U f(\hat{\mathbf{U}}, \hat{\mathbf{B}})$
- 16: Projection for $\hat{\mathbf{U}}$: $\hat{\mathbf{U}}^+ \stackrel{\text{QR}}{\leftarrow} \mathbf{U} + \mathbf{R}^+$. Set $\hat{\mathbf{U}}_t \leftarrow \mathbf{U}^+$.
- 17: **EXIT loop if** $\text{SD}(\hat{\mathbf{U}}_{t-1}, \hat{\mathbf{U}}_t)/\sqrt{\hat{r}} < \epsilon_{exit} = 0.01$.
- 18: **end for**
- 19: **Output:** $\hat{\mathbf{X}} := [\hat{\mathbf{x}}_1, \hat{\mathbf{x}}_2, \dots, \hat{\mathbf{x}}_q]$.

MRI setting. In our current setting of $\mathbf{A}_k = \mathbf{H}_k \mathbf{F}$, the following can be shown. If the nonzero entry of each row of \mathbf{H}_k is selected using the i.i.d. Bernoulli(ρ) model, then one can also show that $\mathbb{E}[\frac{1}{\rho} \mathbf{X}_{0, full}] = \mathbf{X}^*$. Here we are assuming that \mathbf{F} is scaled so that $\mathbf{F}^\top \mathbf{F} = \mathbf{I}$. This is the intuitive reason why the above initialization also works for the MRI setting. When $m_k \neq m_1$ (time varying number of measurements), based on theory (see Appendix B), one needs to replace the $1/m$ factor by $1/\sqrt{m_k \bar{m}}$ where $\bar{m} = \sum_{k=1}^q m_k/q$. In the MRI setting, all m_k 's are very similar, so either choice works equally well.

B. Setting parameters in practical settings

The algorithm parameters are the rank r , the truncation threshold \tilde{C} for the initialization matrix, the GD step size η , and the maximum number of iterations T along with a stopping criterion to exit the loop sooner if the estimates do not change much. We set these as explained below.

To set r , we directly explain how to do it for approximately LR matrices since all real image sequences are only approximately LR. In this case, there is no one correct choice to use.

We use the following constraints to find a good approach. We need our choice of rank, \hat{r} , to be sufficiently small compared to $\min(n, q)$ for the algorithm to take advantage of the LR assumption. Moreover, for the LS step for updating $\hat{\mathbf{b}}_k$'s to work well (for its error to be small), we also need it to also be small compared with m . One approach that is used often is to use the “ $b\%$ energy threshold” on singular values. This computes \hat{r} as the smallest value of r for which $\sum_{j=1}^r \sigma_j^2 \geq (b/100) \cdot \sum_{j=1}^{\min(n,q)} \sigma_j^2$. Here σ_j should be the j -th singular value of \mathbf{X}^* , but since \mathbf{X}^* is unknown, we use the initialization matrix $\hat{\mathbf{X}}_0$ as its estimate. Thus, one good heuristic that respects the above constraints is to compute the “ $b\%$ energy threshold” of the first $\min(n, q, m)/10$ singular values, i.e. compute \hat{r} as the smallest value of r for which

$$\sum_{j=1}^{\hat{r}} \sigma_j(\mathbf{X}_0)^2 \geq (b/100) \cdot \sum_{j=1}^{\min(n,q,m)/10} \sigma_j(\mathbf{X}_0)^2.$$

for a $b \leq 100$. We use $b = 85$ in all our experiments, but any large value can be used instead. The algorithm is not sensitive to this choice.

We set the GD step size $\eta = 0.14/\|\nabla_U f(\hat{\mathbf{U}}_0, \hat{\mathbf{B}}_0)\|$ where $\hat{\mathbf{U}}_0, \hat{\mathbf{B}}_0$ are the initial estimates. Assuming that the gradient norm decreases over iterations, this implies that $\eta \cdot \|\nabla_U f(\hat{\mathbf{U}}_t, \hat{\mathbf{B}}_t)\| \leq 0.14 < 1$ always. Since $\|\hat{\mathbf{U}}_t\| = 1$ (due to the QR decomposition step), this ensures that a GD step is never too big. We use $\tilde{C} = 36$ in the initialization step. To decide T (maximum number of iterations), we stop the GD loop when $\text{SD}(\hat{\mathbf{U}}_{t-1}, \hat{\mathbf{U}}_t) < \epsilon_{exit} \sqrt{\hat{r}}$ while setting $T_{max} = 70$ so that no more than 70 iterations are run. We set $\epsilon_{exit} = 0.01$.

The above algorithm is summarized in Algorithm 1.

Other parameter setting approaches. As suggested in [10], one can also set η as $\eta = c/(m\|\hat{\mathbf{U}}_0 \hat{\mathbf{B}}_0\|^2)$ with a $c < 1$. This is a conservative approach that is needed for proving guarantees which are only sufficient conditions and will lead to slower convergence. Motivated by theory [10], we could set $\tilde{C} = 6 \max_k \|\mathbf{y}_k\|^2 / (\sum_{k=1}^q \|\mathbf{y}_k\|^2 / q)$.

C. Implementation

We write things as above only for ease of explanation. In our implementation, we never use matrix-vector multiplication for computing $\mathbf{A}_k \mathbf{x}$ or $\mathbf{A}_k^\top \mathbf{y}$, since that is much more memory intensive and much slower than using Fast FT (FFT). Also, we use various MATLAB features and linear algebra tricks to remove “for” loops wherever possible. Code is provided at the links given in Sec. VI.

IV. SOLVING APPROXIMATE-LRCCS FOR DYNAMIC MRI

We develop algorithms under two possible approximate LRcCS models.

A. altGDmin-MRI: altGDmin with mean subtraction and unstructured Modeling Error Correction (MEC)

Recall the approx-LRcCS modeling assumption from Sec. II-C. We assume $\mathbf{z}_k^* = \tilde{\mathbf{z}}^* + \mathbf{x}_k^* + \mathbf{e}_k^*$ with $\|\mathbf{e}_k^*\| \ll \|\mathbf{x}_k^*\| \ll \|\tilde{\mathbf{z}}^*\|$. We first explain why we expect this model to be better for accurate reconstruction in highly understampled settings. For an $r \ll n, q$, the condition number for the rank- r approximation of \mathbf{X}^* , $\kappa_{\mathbf{X}^*, r}$ is much lower than

Algorithm 2 *altGDmin-MRI: altGDmin with mean subtraction and unstructured MEC. CGLS is the code from [44].*

- 1) Solve $\min_{\bar{\mathbf{z}}} \sum_{k=1}^q \|\mathbf{y}_k - \mathbf{A}_k \bar{\mathbf{z}}\|^2$ using CGLS with tolerance 10^{-36} and maximum number of iterations 10. Denote solution by $\hat{\bar{\mathbf{z}}}$.
 - 2) For each $k \in q$, compute $\tilde{\mathbf{y}}_k := \mathbf{y}_k - \mathbf{A}_k \hat{\bar{\mathbf{z}}}$.
 - 3) Run Algorithm 1 (auto-altGDmin) with $\tilde{\mathbf{y}}_k, \mathbf{A}_k$ as its inputs.
 - 4) For each $k \in q$, compute $\tilde{\tilde{\mathbf{y}}}_k := \mathbf{y}_k - \mathbf{A}_k \hat{\bar{\mathbf{z}}} - \mathbf{A}_k \hat{\mathbf{x}}_k$.
 - 5) For each $k \in q$, starting with a zero initialization, run 3 iterations of CGLS to solve $\min_e \|\tilde{\tilde{\mathbf{y}}}_k - \mathbf{A}_k e\|^2$. Denote the output by \hat{e}_k .
- Output $\hat{\mathbf{Z}} := [\hat{\mathbf{z}}_1, \hat{\mathbf{z}}_2, \dots, \hat{\mathbf{z}}_q]$ with $\hat{\mathbf{z}}_k = \hat{\bar{\mathbf{z}}} + \hat{\mathbf{x}}_k + \hat{e}_k$.

the rank- $(r+1)$ condition number of \mathbf{Z}^* , $\kappa_{\mathbf{Z}^*, r+1}$ ³. For example, for the PINCAT sequence, it decreases from 17.1 to 3.4 after subtracting the average image, while for the vocal tract sequence it decreases from 8.8 to 2.5. Here we used $r = \min(n, q)/10$. From our theoretical guarantees [10] briefly summarized in Appendix B (Supplementary Material), the sample complexity grows as κ^4 . While this result is for random Gaussian measurements, it is known from the (sparse) Compressive Sensing literature, that the qualitative implications of analysis for the Gaussian case also hold for random Fourier settings. We expect a similar implication also for LRcCS. Thus, a lower κ means a smaller value of m suffices to get an accurate reconstruction. Or, in other words, when m is small, smaller κ implies a better reconstruction accuracy. This is indeed validated in our experiments given later; see Table I.

We proceed as follows. We estimate $\bar{\mathbf{z}}^*$ by solving the following LS problem:

$$\min_{\bar{\mathbf{z}}} \sum_{k=1}^q \|\mathbf{y}_k - \mathbf{A}_k \bar{\mathbf{z}}\|^2.$$

Denote the solution by $\hat{\bar{\mathbf{z}}}$. We expect this step to work well since the “noise” seen by this step is $\mathbf{x}_k^* + e_k^*$ and, by assumption, this is small compared to $\bar{\mathbf{z}}^*$. Next, we estimate \mathbf{X}^* by using the measurement residuals

$$\tilde{\mathbf{y}}_k := \mathbf{y}_k - \mathbf{A}_k \hat{\bar{\mathbf{z}}}$$

as the input to altGDmin. Denote its output by $\hat{\mathbf{X}}$. The last step, which we refer to as Modeling Error Correction (MEC) is to estimate the unstructured e_k^* by using the new measurement residuals

$$\tilde{\tilde{\mathbf{y}}}_k := \mathbf{y}_k - \mathbf{A}_k \hat{\bar{\mathbf{z}}} - \mathbf{A}_k \hat{\mathbf{x}}_k$$

³For this discussion, assume that $e_k^* = 0$ for all k . Since $\bar{\mathbf{z}}^* = \sum_k \mathbf{z}_k^*/q$, thus $\sum_k \mathbf{x}_k^* = 0$. Thus, $\mathbf{Z}^* \mathbf{Z}^{*\top} = q \bar{\mathbf{z}}^* \bar{\mathbf{z}}^{*\top} + \mathbf{X}^* \mathbf{X}^{*\top}$. Let $\mathbf{w}_1 := \bar{\mathbf{z}}^*/\|\bar{\mathbf{z}}^*\|$. $\mathbf{Z}^* \mathbf{Z}^{*\top} \mathbf{w}_1 = \mathbf{w}_1 (q \|\bar{\mathbf{z}}^*\|^2) + \sum_k \mathbf{x}_k^* (\mathbf{x}_k^{*\top} \mathbf{w}_1)$. Using $|\mathbf{x}_k^*| \leq \|\mathbf{x}_k^*\|$, each entry of the second term lies in the range $\pm \sum_k \|\mathbf{x}_k^*\|^2$. By our modeling assumption, $\sum_k \|\mathbf{x}_k^*\|^2 \ll q \|\bar{\mathbf{z}}^*\|^2$. Thus, the second term ≈ 0 and so $\mathbf{w}_1 := \bar{\mathbf{z}}^*/\|\bar{\mathbf{z}}^*\|$ is approximately the top eigenvector of $\mathbf{Z}^* \mathbf{Z}^{*\top}$ with eigenvalue $\|\bar{\mathbf{z}}^*\|^2 q$. This further implies that $\lambda_j(\mathbf{X}^* \mathbf{X}^{*\top}) \approx \lambda_{j+1}(\mathbf{Z}^* \mathbf{Z}^{*\top})$ for all $j = 1, 2, \dots, r$. In particular, this means that $\lambda_2(\mathbf{Z}^* \mathbf{Z}^{*\top}) \approx \lambda_1(\mathbf{X}^* \mathbf{X}^{*\top}) \leq \sum_k \|\mathbf{x}_k^*\|^2 \ll q \|\bar{\mathbf{z}}^*\|^2 \approx \lambda_1(\mathbf{Z}^* \mathbf{Z}^{*\top})$. Thus $\kappa_{\mathbf{X}^*, r}^2 := \frac{\lambda_1(\mathbf{X}^* \mathbf{X}^{*\top})}{\lambda_r(\mathbf{X}^* \mathbf{X}^{*\top})} \approx \frac{\lambda_2(\mathbf{Z}^* \mathbf{Z}^{*\top})}{\lambda_{r+1}(\mathbf{Z}^* \mathbf{Z}^{*\top})} \ll \frac{\lambda_1(\mathbf{Z}^* \mathbf{Z}^{*\top})}{\lambda_{r+1}(\mathbf{Z}^* \mathbf{Z}^{*\top})} = \kappa_{\mathbf{Z}^*, r+1}^2$.

and solving

$$\min_e \|\tilde{\tilde{\mathbf{y}}}_k - \mathbf{A}_k e\|^2$$

for each k , while imposing the assumption that $\|e\|^2$ is small. An indirect way to enforce this, while also getting a fast algorithm, is to run only a few iterations of GD to solve this minimization problem.

Stagewise / Hierarchical algorithm interpretation. The above algorithm can be interpreted as a 3-level stage-wise / hierarchical approach:

- 1) Estimating the common mean and subtracting its projections out from each of the \mathbf{y}_k 's is a special case of imposing an LR model with rank $r = 1$ in the first level.
- 2) In the second level, we are imposing a LR model of rank $r = \hat{r}$. We compute \hat{r} as described earlier.
- 3) The third level for recovering e_k^* s individually can be understood as an LR model with rank $r = q$.

Typical stagewise / hierarchical approaches of this type, e.g., [45], start with rank $r = 1$, and keep increasing r and re-running the entire algorithm for the LR model (in our case altGDmin) until a stopping criterion is reached. This can get expensive in practice. Our approach instead uses 3 levels: $r = 1$, $r = \hat{r}$ and $r = q$.

Setting parameters. The parameters for altGDmin are set as explained earlier. We use the Stanford Conjugate Gradient LS (CGLS) code [44] for computing the common-mean (it is an LS problem with mq measurements and n -length unknown vector $\bar{\mathbf{z}}^*$). We used this code with tolerance of 10^{-36} and maximum number of iterations 10. We also used CGLS for the final MEC step. In this case we reduced the maximum number of iterations to 3. This is an indirect way of using the assumption that the residual modeling error has small magnitude.

The complete algorithm is summarized in Algorithm 2.

B. AltGDmin-MRI-2: altGDmin with mean subtraction and (temporal Fourier) sparse MEC

In some applications, using a Fourier sparsity (along the time axis) model on the residual is a better idea than modeling it as an unstructured small magnitude residual. This model imposes temporal smoothness while also allowing some higher temporal frequency signals (non-smooth parts) in the residual. To be precise, we are imposing the following model on the matrix formed by the LR residuals e_k^* 's, \mathbf{E}^* :

$$\mathbf{E}^* := \mathcal{F}_{row}(\mathbf{S}^*)$$

where \mathbf{S}^* is a sparse matrix and \mathcal{F}_{row} applies the 1D discrete Fourier transform (DFT) to each row of \mathbf{S} . We thus have the following model on the images' matrix \mathbf{Z}^* :

$$\mathbf{Z}^* = (\bar{\mathbf{z}}^* \mathbf{1}^\top) + \mathbf{X}^* + \mathbf{E}^*, \quad \mathbf{E}^* := \mathcal{F}_{row}(\mathbf{S}^*)$$

with assuming that $\|\mathbf{E}^*\|_F \ll \|\mathbf{X}^*\|_F \ll \sqrt{q} \|\bar{\mathbf{z}}^*\|$.

The first two steps of the algorithm (mean computation and subtraction followed by altGDmin) are the same as those in the previous section. For the last MEC step, instead of a few iterations of regular GD to estimate the residual e_k , we use the Iterative Soft Thresholding Algorithm (ISTA) for sparse recovery [46] which was also used in [21]. For recovering

Algorithm 3 *altGDmin-MRI2: altGDmin with mean-subtraction and (temporal Fourier) sparse MEC.*

- 1) Run the first 4 steps of Algorithm 2. Let $\tilde{\mathbf{Y}} = [\tilde{\mathbf{y}}_1, \tilde{\mathbf{y}}_2, \dots, \tilde{\mathbf{y}}_q]$.
 - 2) Run the following ISTA algorithm on $\tilde{\mathbf{Y}}$
 - a) $\hat{\mathbf{E}}_0 = \mathbf{0}$.
 - b) Repeat the following for 10 iterations or until $\|\hat{\mathbf{E}}_\tau - \hat{\mathbf{E}}_{\tau-1}\|_F / \|\hat{\mathbf{E}}_{\tau-1}\|_F < 0.0025$

$$\hat{\mathbf{E}}_\tau \leftarrow \mathcal{F}_{row}(\text{SThr}_\omega(\mathcal{F}_{row}^{-1}(\hat{\mathbf{E}}_{\tau-1} + \mathbf{A}^\top(\tilde{\mathbf{Y}} - \mathcal{A}(\hat{\mathbf{E}}))))$$

If \mathbf{W} is the input matrix to $\text{SThr}_\omega(\cdot)$, we use $\omega = 0.001 \cdot \max(\max(\text{abs}(\mathbf{W})))$.

$$\tau \leftarrow \tau + 1$$
- Output $\hat{\mathbf{Z}} := \hat{\mathbf{z}}\mathbf{1}^\top + \hat{\mathbf{X}} + \hat{\mathbf{E}}$.
-

an unknown sparse \mathbf{s} from $\mathbf{y} := \mathbf{A}\mathbf{s}$, this starts with a zero initialization, $\hat{\mathbf{s}} = \mathbf{0}$, and runs the iterations: $\hat{\mathbf{s}} \leftarrow \text{SThr}_\omega(\hat{\mathbf{s}} + \mathbf{A}^\top(\mathbf{y} - \mathbf{A}\hat{\mathbf{s}}))$. Here $\text{SThr}_\omega(\hat{\mathbf{s}})$ zeroes out entries of $\hat{\mathbf{s}}$ that are smaller than ω while shrinking the larger magnitude entries towards zero by ω , i.e. $[\text{SThr}_\omega(\hat{\mathbf{s}})]_i = \text{sign}(\hat{\mathbf{s}}_i)(|\hat{\mathbf{s}}_i| - \omega)$ if $|\hat{\mathbf{s}}_i| > \omega$ and $[\text{SThr}_\omega(\hat{\mathbf{s}})]_i = 0$ otherwise.

For our model, this translates to the following iteration. Compute the residual $\tilde{\mathbf{Y}} := \mathbf{Y} - \mathcal{A}(\hat{\mathbf{z}}\mathbf{1}^\top) - \mathcal{A}(\hat{\mathbf{X}})$. Update $\hat{\mathbf{E}}$ by running the following iteration starting with a zero initialization $\hat{\mathbf{E}} = \mathbf{0}$:

$$\hat{\mathbf{E}} \leftarrow \mathcal{F}_{row}(\text{SThr}_\omega(\mathcal{F}_{row}^{-1}(\hat{\mathbf{E}} + \mathbf{A}^\top(\tilde{\mathbf{Y}} - \mathcal{A}(\hat{\mathbf{E}}))))$$

Setting parameters. We used soft thresholding with threshold $\omega = 0.001 \cdot \max(\max(\text{abs}(\mathbf{W})))$ where \mathbf{W} is the input matrix to $\text{SThr}_\omega(\cdot)$.

The complete algorithm, altGDmin-MRI2, is summarized Algorithm 3.

The temporal Fourier sparsity model has been used for imposing the L+S assumption on dynamic MRI sequences in [21], [22], and follow-up works. We should clarify that, in this work, we are not imposing the L+S model, instead we are assuming a 3-level hierarchical model, with sparsity being used to model the residual in the third level. The assumption $\|\mathbf{E}^*\|_F \ll \|\mathbf{X}^*\|_F$ makes our model different from the regular L+S model which assumes $\mathbf{Z}^* = \mathbf{X}^* + \mathbf{E}^*$ with no assumption on one of them being smaller in magnitude than the other. From our experiments in Sec. VI, in an average sense, altGDmin-MRI2 gives better reconstructions (both in terms of error and visually), but that may also be because the reconstruction algorithms used are different (we use a GD-based algorithm, while [21], [22], use different algorithms to solve the convex relaxation of the L+S model). This issue will be explored in more detail in future work where we plan to also develop a GD-based algorithm under the L+S assumption.

V. MINI-BATCH AND ONLINE ALTGDMIN: SUBSPACE TRACKING BASED SOLUTIONS

The algorithms discussed so far are batch methods, i.e., they require waiting for all the measurements to be taken. This

means they cannot be used in applications that require real-time or pseudo real-time reconstructions, e.g., MRI-guided interventional radiology or real-time vocal tract shaping experiments during speaking (explained in Introduction).

A. Mini-batch Subspace Tracking

Consider the pseudo-real-time setting in which the algorithm processes each new mini-batch of the data (here a set of α consecutive \mathbf{y}_k s) as soon as it arrives. Thus, instead of waiting for all q measurement vectors \mathbf{y}_k to be obtained, it only waits for a new set of α measurements and processes them to return a reconstructed image. For algorithms that use the LR assumption on the data, such an algorithm can be referred to as a *Subspace Tracking* solution since it is implicitly assuming that consecutive mini-batches of data lie in, or close to, the same or slightly different r -dimensional subspaces. One can utilize this “slow subspace change” assumption in the following fashion. For the first mini-batch, use the altgdmin-MRI algorithm with q replaced by α . For later mini-batches, use altgdmin-MRI with two changes. Use the final estimated $\hat{\mathbf{U}}$ from the previous mini-batch, denoted $\hat{\mathbf{U}}^{(j-1)}$, as the initialization for the current one. This means that we replace lines 2-6 of Algorithm 1 by $\hat{\mathbf{U}}_0 \leftarrow \hat{\mathbf{U}}^{(j-1)}$. Second, reduce the maximum number of iterations for the j -th minibatch, denoted $T_{\max,j}$, to a much lower value for $j > 1$ than for $j = 1$.

The complete algorithm is summarized in Algorithm 4. As we will see in Sec. VI-D, besides operating in mini-batch mode, the algorithm speed is also much faster. Even then, the increase in recovery error is insignificant until $\alpha = 64$.

B. Online Subspace Tracking

In certain other applications, after an initial short delay, a true real-time (fully online) algorithm is needed. This means, each time a new \mathbf{y}_k is obtained, it should return a new estimate $\hat{\mathbf{x}}_k$. To obtain such an algorithm we eliminate the mean computation step and the \mathbf{U} update steps from the original algorithm. Suppose the first mini-batch consists of α_1 frames. For all times $k > \alpha_1$, we use the estimated mean $\bar{\mathbf{z}}$ and the estimated $\hat{\mathbf{U}}$ from the first mini-batch. For $k > \alpha_1$, for each new \mathbf{y}_k , we only update \mathbf{b}_k and \mathbf{e}_k . This can be understood as mini-batch ST with $\alpha_j = 1$ and $T_j = 1$ for $j > 1$. We summarize this algorithm in Algorithm 5.

VI. EXPERIMENTS

The code for all experiments in this paper will soon be posted at https://github.com/Silpa1/comparison_of_algorithms.

Algorithm 4 *Mini-batch Subspace Tracking*

- 1) Let $j = 1$. Run Algorithm 2 on first mini-batch of α_1 \mathbf{y}_k s. Thus $q \equiv \alpha_1$ and we let $T_{\max,1} = 70$. Denote its final subspace estimate by $\hat{\mathbf{U}}^{(1)}$.
- 2) For $j > 1$ do
 - a) Run Algorithm 2 with the following changes: (i) replace the Initialization step of altGDmin (Algorithm 1) by $\hat{\mathbf{U}}_0 \leftarrow \hat{\mathbf{U}}^{(j-1)}$; and (ii) set $T_{\max,j} = 5$. Denote its final subspace estimate by $\hat{\mathbf{U}}^{(j)}$.

End For

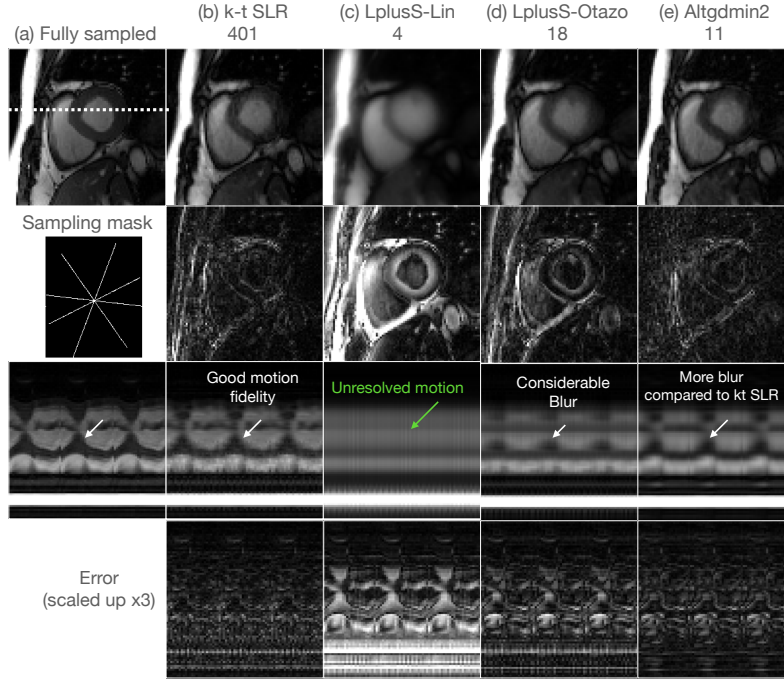


Fig. 3: Visually comparing one OCMR cardiac sequence [47] with retrospective undersampling with 4 radial lines/frame. Image time profile along the white dotted line in (a) along with the sampling mask are shown in the second row. Images are repeated by a factor 3 along time to better visualize the motion. Error images are calculated as difference between fully sampled and reconstructed images. We observe loss in image quality in all algorithms due to the high undersampling factor. However, L+S-Lin and L+S-Otazo show substantially higher motion blur compared to ktSLR and AltGDmin-MRI2 (AltGDmin2). In comparison to ktSLR, altGDmin2 shows slightly higher blur in this dataset.

Algorithm 5 Online Subspace Tracking

- 1) For the first mini-batch of α frames, run Algorithm 2. Denote the computed mean image by $\hat{z}_{(1)}$ and the final subspace estimate by $\hat{U}^{(1)}$.
- 2) For $k > \alpha + 1$ do:
 - a) Compute $\tilde{y}_k = y_k - A_k \hat{z}_{(1)}$
 - b) Let $\hat{U} = \hat{U}^{(1)}$.
 - c) Compute $\hat{b}_k \leftarrow (A_k \hat{U})^\dagger \tilde{y}_k$.
 - d) Compute $\tilde{y}_k = \tilde{y}_k - A_k \hat{U} \hat{b}_k$
 - e) Compute e_k by running 3 iterations of CGLS to solve $\min_e \|\tilde{y}_k - A_k e\|^2$. Denote the output by \hat{e}_k .
 - f) Output $\hat{x}_k = \hat{z}_{(1)} + \hat{U} \hat{b}_k + e_k$

End For

Dataset (# lines)	only Mean	only altGDmin	Mean+altGDmin	altGDmin-MRI
PINCAT (16)	0.0711	0.0393	0.0162	0.0096
short-speech (16)	0.2018	0.1674	0.1024	0.0720
cardiac-cine (16)	0.0089	0.0245	0.0060	0.0057
long-speech (16)	0.2440	0.1879	0.1236	0.0948
cardiac-fb (4)	0.3496	0.3768	0.2305	0.2267
cardiac-fb (8)	0.3197	0.2825	0.1594	0.1487
cardiac-fb (16)	0.3143	0.2170	0.1385	0.1167

TABLE I: Understanding the effect of the various steps of altGDmin-MRI. We report **Error** as defined in Sec. VI (first para).

The error value that we report in all experiments is normalized scale-invariant mean squared error (N-S-MSE) computed as follows $Error = (\sum_{k=1}^q \text{dist}^2(\mathbf{x}_k^*, \hat{\mathbf{x}}_k)) / \|\mathbf{X}^*\|_F^2$ where $\text{dist}^2(\mathbf{x}^*, \hat{\mathbf{x}}) = \|\mathbf{x}^* - \hat{\mathbf{x}} \frac{\|\mathbf{x}^*\|}{\|\hat{\mathbf{x}}\|}\|^2$ is the scale invariant distance between two vectorized images with “scale” being a complex number (the reconstructed images can be complex-valued). We also report the time taken to recover the entire sequence in

seconds. The reporting format is **Error (Time in seconds). In the last row of most tables, we display the average-error (average-time) which computes the average error or time over all previous rows.**

We show experiments for 8 retrospectively undersampled single and multi-coil dynamic MRI applications with multiple undersampling rates and sampling patterns (2D pseudo-radial or 1D-Cartesian: (i) multi parameter ($T2 - T1\rho$) brain sequence (brain) [21], [22], (ii) free breathing un-gated cardiac perfusion (cardiac-fb) [24] (this had both perfusion dynamics and motion dynamics due to cardiac and breathing motion), (iii) free breathing PINCAT perfusion phantom (PINCAT) [4], [22] (containing dynamics due to perfusion uptake in the heart as well as heavy breathing motion), (iv) a short 59-frame speech sequence acquired on a University of Iowa volunteer speaking slowly (short-speech), (v) one breath-held cardiac sequence from the OCMR database [47] (cardiac-cine), (vi) a high temporal resolution (2048-frame) but low spatial resolution speech sequence acquired at the University of Iowa on a healthy volunteer (long-speech), (vii) Cartesian undersampled breath-held cardiac cine sequence from [21], [22], and (viii) Cartesian undersampled breath-held cardiac perfusion sequence from [21], [22]. Details of these datasets are provided in the Supplement in Appendix C. The undersampling is either 2D golden-angle based pseudo-radial⁴ or 1D Cartesian (using the sampling scheme of [21]) or true

⁴The angular increment between successive radial spokes is determined by the golden angle (111.25 degrees) [48]. The starting point is changed over time so that the sampling masks are different for different images in the sequence. The golden angle ensures maximum incoherent kspace coverage over time.

Dataset (# lines)	ktSLR	L+S-Otazo	L+S-Lin	altGDmin-MRI	altGDmin-MRI2	DL
brain-T2-T1(4)	0.0676 (15.52)	0.0210 (3.61)	0.0875 (1.04)	0.0212 (0.51)	0.0212 (0.58)	
brain-T2-T1(8)	0.0227 (14.60)	0.0101 (1.99)	0.0151 (1.02)	0.0101 (0.57)	0.0101 (0.55)	
brain-T2-T1(16)	0.0094 (12.82)	0.0046 (1.37)	0.0046 (0.94)	0.0052 (0.55)	0.0052 (0.57)	
Cardiac-ocmr-data(4)	0.1425 (29.32)	0.0818 (6.76)	0.1731 (1.82)	0.0249 (2.60)	0.0252 (3.47)	
Cardiac-ocmr-data(8)	0.0704 (28.76)	0.0232 (6.70)	0.0965 (1.85)	0.0102 (2.59)	0.0102 (3.52)	
Cardiac-ocmr-data(16)	0.0100 (29.03)	0.0063 (5.23)	0.0236 (1.82)	0.0057 (2.41)	0.0057 (2.48)	0.06
speech-seq(4)	0.1876 (24.25)	0.2229 (6.16)	0.1947 (1.70)	0.1836 (2.17)	0.1939 (2.88)	
speech-seq(8)	0.0936 (23.57)	0.0764 (6.20)	0.0914 (1.68)	0.1133 (1.61)	0.1131 (1.63)	
speech-seq(16)	0.0470 (17.15)	0.0414 (4.50)	0.0441 (1.65)	0.0713 (1.19)	0.0711 (1.21)	
FB-ungated(4)	0.3854 (108.96)	0.3400 (25.71)	0.4569 (7.29)	0.2383 (7.68)	0.2382 (8.05)	
FB-ungated(8)	0.2507 (109.19)	0.1721 (25.53)	0.2981 (7.33)	0.1499 (6.16)	0.1497 (6.55)	
FB-ungated(16)	0.1539 (107.67)	0.1058 (24.02)	0.1568 (7.31)	0.1177 (4.33)	0.1174 (4.56)	
lowres-speech(4)	0.2418 (261.76)	0.2496 (733.64)	0.4171 (360.95)	0.1704 (33.31)	0.1679 (44.82)	
lowres-speech(8)	0.1758 (523.70)	0.1770 (722.61)	0.2395 (356.00)	0.1224 (45.77)	0.1208 (62.10)	
lowres-speech(16)	0.1183 (182.14)	0.1277 (632.37)	0.1331 (362.05)	0.0952 (43.81)	0.0952 (44.51)	
Pincat(4)	0.0445 (34.85)	0.0381 (8.04)	0.1054 (2.26)	0.0278 (1.63)	0.0278 (1.77)	
Pincat(8)	0.0216 (31.54)	0.0162 (3.91)	0.0208 (2.22)	0.0166 (1.36)	0.0166 (1.31)	
Pincat(16)	0.0095 (23.31)	0.0065 (2.70)	0.0047 (2.25)	0.0097 (1.08)	0.0097 (1.13)	
avg-Error (avg-time)	0.1140 (87.67)	0.0956 (123.39)	0.1424 (62.28)	0.0774 (8.85)	0.0777 (10.64)	

TABLE II: **Single-coil comparisons:** Comparing ktSLR [4], L+S-Otazo [21], L+S-Lin [22], altGDmin [10], altGDmin-MRI and altGDmin-MRI2 and the Deep Learning (DL) algorithm of [29], for 6 very different dynamic MRI sequences pseudo-radially undersampled using 16, 8, and 4 radial lines. For ktSLR and L+S-Otazo, we used the parameters for cardiac. For L+S-Lin we did two experiment: the first was using parameters for cardiac, the second used parameters for PINCAT (both were provided by authors). We provide the full table with sets of results in Table VI in the Supplement Appendix. We report **Error (Time in seconds)** with Error defined in the beginning of Sec. VI. The last row shows the **avg-Error (avg-Time)**, with average being taken over all 18 previous rows. Image sequence sizes: PINCAT ($n = 16384, 50$), Brain ($n = 16384, q = 24$), Vocal tract ($n = 10000, q = 59$), Cardiac-cine ($n = 27648, q = 25$), lowres-speech ($n = 3600, q = 2048$), cardiac-free-breathing (cardiac-fb) ($n = 31104, q = 80$).

radial. Radial sampling provides a way to non-uniformly undersample the 2D Fourier plane in such a way that more samples are acquired in the center of the 2D Fourier plan (low frequency regions in both dimensions). However directly using radially sampled data in the reconstruction algorithm requires use of the computationally expensive non-uniform FT (NUFT) which makes the algorithm very slow. Previous research has shown negligible loss in image quality if the polar coordinates of radially undersampled data are regridded onto the Cartesian grid (polar coordinates interpolated onto rectangular ones), followed by use of fast FT (FFT) algorithms in iterative constrained reconstruction algorithms [7], [8], [9]. In fact, for Compressive Sensing based methods, there is sometimes an improvement in reconstruction quality as well and we observe this too in our experiments. This type of data – radially sampled data mapped onto the Cartesian grid is called “pseudo-radial” k-space data, and motivated our choice of sampling in retrospective undersampling experiments. We also show reconstructions on two open-source prospectively radially undersampled datasets in the Supplement and in Sec. VI-E.

Our experiments included results on radial undersampling with 16, 8, and 4 radial lines. The use of f radial lines means $m_k \approx (f/128) \cdot n$ or that the acceleration is roughly $(128/f)$. Thus 16 radial lines means 8x acceleration while 4 lines means 32x acceleration.

All experiments were conducted in MATLAB on the same PC. AltGDmin-MRI and altGDmin-MRI2 were compared with the two provable techniques – mixed norm min [13], altMin (changed for the current linear setting) [45]; with 3 state-of-the-art methods from dynamic MRI literature that rely on structural assumptions (sparsity or LR or both) – ktSLR [4], L+S-Otazo [21], L+S-Lin [22]; and with one deep learning (DL) approach trained on the cardiac-cine dataset [29]. For

all comparisons, we used author provided code (ktSLR: emailed by the author to us, L+S-Lin: downloaded from <https://github.com/JeffFessler/reproduce-l-s-dynamic-mri>, and L+S-Otazo: obtained from <https://cai2r.net/resources/ls-reconstruction-matlab-code/>). In all these codes, the input k-space data is needed in a different format (the sequence of frequency locations is different, due to different uses of the “fftshift” in MATLAB). To deal with this, we converted all algorithms so that all of them took input kspace data in the same format as L+S-Lin. We wrote our own code to also match this. This was done by using the getE function from <https://github.com/JeffFessler/reproduce-l-s-dynamic-mri> in our code-writing (this computes $\mathcal{A}(\mathbf{X}^*)$ and its adjoint in an efficient fashion for MATLAB) and also in the code of L+S-Otazo and ktslr. Doing this, significantly improved the L+S-Otazo performance and did not change anything for ktSLR.

Most of the algorithms except ours have parameter settings that require the input kspace data to be normalized in a certain fashion even for the algorithm to work. On the other hand, for all versions of altGDmin, the input parameters are set in such a way that this is not required.

A. Comparison with the 2 provable algorithms: mixed norm min and AltMin

Both AltMin and the convex relaxation (mixed norm min) were much slower and had larger errors. We provide the results in the Supplement.

B. Comparisons for Retrospective single-coil dynamic MRI

Comparing various steps of altGDmin-MRI. Before doing a detailed comparison with existing works, we try to understand the utility of each of the steps of altGDmin-MRI. In Table I, we report results for just computing the mean image and using $\hat{\mathbf{x}}_k = \hat{\mathbf{z}}$ for all $k \in [q]$ (only Mean), just using altGDmin on

the measurements \mathbf{y}_k (only altGDmin), use of both of these (Mean+altGDmin) and use of all three steps (altGDmin-MRI). Observe that, in terms of reconstruction error, in most cases, just altGDmin is better than just mean. In terms of recovered image quality, mean will always be worse. Use of both steps – mean subtraction followed by altGDmin – improves the error significantly compared to either of them in all cases. Finally use of the modeling error correction (MEC) step improves recovery errors especially in the 16 radial lines’ setting. This step is needed for significantly improved reconstructed image sequence visual quality. In later experiments, we only altGDmin-MRI and altGDmin-MRI2.

Comparisons with existing state of the art. We compared altGDmin-MRI and altGDmin-MRI2 with kt-SLR, L+S-Otazo, and L+S-Lin, for 6 sequences and 3 choices of numbers of radial lines: 4, 8, and 16, thus there were a total of 18 datasets. We report the **Error (Time)** in Table II. As can be seen, in most cases, altGDmin-MRI and altGDmin-MRI2 (use of sparse MEC) have the lowest errors. In cases when the altGDmin-MRI error is not the lowest, it is very close to the lowest. In the last row of this table, we display the average-error (average-time). Observe that our approaches have the best errors and are also the fastest. For L+S-Lin, we evaluated it with using parameters specified for cardiac data and with parameters specified for PINCAT. Overall the cardiac parameters gave better errors and hence we report results for this case in this section and in all other experiments described below. For L+S-Otazo and ktSLR, cardiac parameters were used also since these gave the best results. We added the full table in Supplement as Table VI.

Comparison with one DL algorithm. We also compare with one Deep Learning (DL) algorithm [29] on the cardiac ocmr dataset with 16 radial lines. The results are provided in the last column of Table II. Since this was trained on 2D images, it reconstructs on a frame-by-frame basis. It does not use time series correlations and hence its reconstruction error is much larger even on a new sequence from the cardiac-cine dataset itself. Training was conducted on GPU (NVIDIA GEFORCE RTX 2080 Ti) with 12 GB memory, training time was approximately 3 hours 10 minutes. The testing (reconstruction) time taken was 2.075 seconds for this sequence.

C. Comparisons for multi-coil retrospectively undersampled dynamic MRI: Cartesian and pseudo-radial

We did the same comparison as above for retrospectively undersampled multi-coil dynamic MRI datasets with $mc = 8$ or 12 coils. We used 15 pseudo-radially undersampled datasets (5 applications, 3 acceleration rates) and we used 2 more datasets taken from [22] which were retrospectively undersampled using 1D Cartesian undersampling (cardiac-perf-Cartesian and cardiac-cine-Cartesian). Dataset details are provided in the Supplement in Appendix C. Error and time-taken comparisons for all the above 17 datasets are reported in Table III, and we provide an average error (average time) row at the end. Altgdmin-MRI and MRI2 are still the best two algorithms both in terms of average-error and average-time. However gap with respect to the other compared methods is not as much as in the single-coil case, and on a row by row

basis it is sometimes not the best approach. We believe the reason is that these other algorithms have parameters tuned for the multicoil setting. Visual comparisons for some of these datasets are shown in Figs. 2, 1, 3. *Visually (and error-wise), altGDmin-MRI2 has either the best or a close second-best reconstruction quality – both error-wise and visual – in all cases, while also being very fast (it is not always the fastest, but it is the fastest for long sequences and fast-enough for all).*

ktSLR has the best errors and best visual performance for most of the pseudo-radial datasets. For these, altGDmin-MRI2 is either as good or slightly worse. But ktSLR has very large error for the Cartesian undersampled ones and it is very slow compared to all the other approaches. It is also the slowest algorithm. L+S-Otazo and L+S-Lin have the best errors for the Cartesian ones (this was data originally provided by authors of this code), but it has larger errors in some of the pseudo-radial cases. For 4 radial lines (32x undersampling), altGDmin-MRI or MRI2 errors are the lowest.

D. Subspace tracking algorithms evaluation

We evaluate these algorithms on the multi-coil long but low-resolution speech sequence with 16 or 4 radial lines. For this sequence, $q = 2048$. We provide the results in Table IV. We evaluate mini-batch ST (Algorithm 4), with $T_{max,1} = 70$ and $T_{max,j} = 5$ for $j > 1$ for decreasing values of α : $\alpha = q = 2048$ (batch setting) and $\alpha = 512, 128, 64, 32, 16$. Observe that for mini-batch sizes up to $\alpha = 64$, there is no appreciable increase in error. But the improvement in reconstruction time is very significant. It is much faster than any of the other algorithms compared in Table III. We also compare with full online ST (Algorithm 5). In this case, there is a significant increase in error as the value of initial mini-batch α decreases. But the speed is even better. Thus, a combination of the mini-batch and online approaches would be the most useful algorithm in practice: work in online mode to obtain real-time reconstructions which are not very accurate; but follow it up with mini-batch updates of the same frames that are much more accurate.

We show visual quality comparison in Fig. 1, last column. As can be seen, the quality as good or better than that of the full batch one. The reason is this approach is modeling a slowly changing subspace rather than a fixed one, and this can be a better assumption for speech sequences.

E. Prospectively undersampled datasets: true radial vs pseudo-radial recon

We used altGDmin-MRI2 to reconstruct two open-source prospectively radially undersampled radial datasets – abdomen and free breathing ungated cardiac perfusion. We did these in two ways (i) by directly using the radial undersampled data and using the NUFT-based code, and (ii) by pre-gridding the data onto the Cartesian grid followed by use of FFT-based code from earlier experiments. The algorithm parameters remained the same in both cases, only the forward and backward (adjoint) operators were differently coded. For NUFT and its inverse we used the non-uniform Fast FT (NUFFT) code from [49]. As can be seen from Appendix D of Supplement, the pre-gridded reconstruction is of better quality and faster. This will be explored in detail in future work.

Dataset	ktslr	L+S-Otazo	L+S-Lin	altGDmin-MRI	altGDmin-MRI2
Cartesian					
cardiac-perf-R8	0.4067 (636.56)	0.0139 (25.22)	0.0241 (15.75)	0.0121 (38.20)	0.0113 (41.70)
cardiac-cine-R6	0.0909 (433.22)	0.0044 (16.92)	0.0053 (6.03)	0.0040 (12.25)	0.0035 (15.02)
Pseudo-radial					
brain-T2-T1rho(4)	0.0093 (140.56)	0.0167 (6.08)	0.0173 (2.73)	0.0125 (3.89)	0.0127 (4.44)
brain-T2-T1rho(8)	0.0034 (112.05)	0.0086 (4.42)	0.0095 (2.62)	0.0054 (4.14)	0.0056 (4.43)
brain-T2-T1rho(16)	0.0014 (83.14)	0.0049 (3.05)	0.0062 (2.66)	0.0027 (3.93)	0.0028 (4.22)
multi-coil-lowres-speech(4)	0.1543 (5337.16)	0.1991 (531.55)	0.2545 (307.65)	0.1533 (110.62)	0.1405 (191.76)
multi-coil-lowres-speech(8)	0.0593 (5300.11)	0.1107 (481.12)	0.1284 (316.48)	0.1154 (146.76)	0.0962 (201.78)
multi-coil-lowres-speech(16)	0.0203 (5251.81)	0.0550 (412.67)	0.0557 (314.36)	0.0773 (203.85)	0.0546 (246.33)
multicoil-ungated-cmr-perf(4)	0.0894 (4222.61)	0.0910 (191.85)	0.1424 (51.37)	0.0695 (71.40)	0.0685 (96.71)
multicoil-ungated-cmr-perf(8)	0.0442 (3540.89)	0.0591 (122.46)	0.0632 (52.23)	0.0470 (67.59)	0.0452 (90.07)
multicoil-ungated-cmr-perf(16)	0.0206 (2848.86)	0.0370 (87.92)	0.0329 (50.42)	0.0298 (65.06)	0.0278 (90.26)
fs-0016-3T-ksp-csm(4)	0.0362 (223.54)	0.0293 (10.35)	0.0515 (2.73)	0.0092 (10.27)	0.0097 (13.05)
fs-0016-3T-ksp-csm(8)	0.0045 (222.36)	0.0064 (8.37)	0.0101 (2.65)	0.0033 (6.97)	0.0036 (6.87)
fs-0016-3T-ksp-csm(16)	0.0015 (159.20)	0.0035 (4.59)	0.0030 (2.79)	0.0015 (5.06)	0.0016 (5.29)
fs-0019-3T-ksp-csm(4)	0.0216 (401.26)	0.0251 (18.50)	0.0698 (4.95)	0.0095 (11.36)	0.0099 (11.62)
fs-0019-3T-ksp-csm(8)	0.0043 (405.82)	0.0092 (12.73)	0.0149 (4.88)	0.0051 (10.18)	0.0053 (10.54)
fs-0019-3T-ksp-csm(16)	0.0020 (265.02)	0.0052 (6.98)	0.0044 (4.91)	0.0032 (9.03)	0.0033 (9.62)
avg-Error (avg-Time)	0.0571 (1740.2)	0.0399 (114.39)	0.0525 (67.36)	0.0330 (45.91)	0.0295 (61.39)

TABLE III: **Multi-coil comparisons:** Comparisons for 5 dynamic MRI sequences (for different applications) psuedo-radially undersampled using 16, 8, and 4 radial lines, and for 2 different datasets that are Cartesian undersampled and taken from [21], [22]. Image sequence sizes: cardiac-perf-R8 ($n = 16384, q = 40$), cardiac-cine-R6 ($n = 65536, q = 24$), brain-T2-T1rho ($n = 16384, q = 24$), multi-coil-lowres-speech ($n = 4624, q = 2048$), multicoil-ungated-cmr-perf ($n = 31104, q = 200$), fs-0016-3T-ksp-csm ($n = 28800, q = 15$), fs-0019-3T-ksp-csm ($n = 27648, q = 25$). Table format is **Error (Time)**. The last row contains the **average-Error (average-Time)** over all 17 rows of results.

α	Mini-batch ST (70,5)	Online ST
16 radial lines		
512	0.0575 (186.35)	0.0895 (131.06)
256	0.0578 (149.58)	0.1139 (89.65)
64	0.0584 (85.75)	0.1468 (39.54)
32	0.0589 (63.28)	0.1613 (32.09)
4 radial lines		
256	0.1201 (83.49)	
64	0.1195 (63.01)	

TABLE IV: *Subspace Tracking results for the low-resolution speech sequence with 16 and 4 radial lines. Mini-batch ST (70,5) is Algorithm 4 with $T_{max,1} = 70$ and $T_{max,j} = 5$ for $j > 1$.*

VII. CONCLUSIONS AND FUTURE WORK

We developed a fast, memory-efficient, and “general” algorithm for accelerated/undersampled dynamic MRI by assuming an approximate LR model on the matrix formed by the vectorized images of the sequence. Here, “general” means that it works with the same set of parameters for multiple MRI applications. Via extensive experiments we show that, on average, our proposed algorithms, altGDmin-MRI and altGDmin-MRI2, outperform a large number of existing approaches while also being faster. We also developed an altGDmin-MRI-based subspace tracking solution that operates in mini-batch mode and showed that it provides comparable reconstruction quality while being even faster. Future work will explore reconstruction of 3D+t data (multi-slice dynamic imaging) using a tensor-based modification of our ideas, and detailed evaluation of our approaches on prospective data. The 3D+t experiments will exploit the memory-efficiency of our algorithms. A second goal will be to develop a GD-based L+S algorithm and evaluate it for different applications.

VIII. *

Acknowledgements We thank Mr. Wahidul Alam who is a graduate student in the BME department at University of Iowa for their assistance on providing reconstruction of one OCMR dataset using a deep learning algorithm. The code for our basic altGDmin algorithm used as its starting point the

matrix-vector code written for the simulated random Gaussian setting by Dr. Seyedehsara (Sara) Nayer who graduated from Iowa State University in 2021.

REFERENCES

- [1] M. Lustig, D. Donoho, and J. M. Pauly, “Sparse MRI: The application of compressed sensing for rapid mr imaging,” *Magnetic Resonance in Medicine*, vol. 58(6), pp. 1182–1195, December 2007.
- [2] U. Gamper, P. Boesiger, and S. Kozerke, “Compressed sensing in dynamic MRI,” *Magnetic Resonance in Medicine*, vol. 59(2), pp. 365–373, January 2008.
- [3] Z.-P. Liang, “Spatiotemporal imaging with partially separable functions,” in *2007 4th IEEE international symposium on biomedical imaging: from nano to macro*, 2007, pp. 988–991.
- [4] S. G. Lingala, Y. Hu, E. DiBella, and M. Jacob, “Accelerated dynamic mri exploiting sparsity and low-rank structure: kt slr,” *Medical Imaging, IEEE Transactions on*, vol. 30, no. 5, pp. 1042–1054, 2011.
- [5] M. Chiew, S. M. Smith, P. J. Koopmans, N. N. Graedel, T. Blumensath, and K. L. Miller, “k-t faster: acceleration of functional mri data acquisition using low rank constraints,” *Magnetic resonance in medicine*, vol. 74, no. 2, pp. 353–364, 2015.
- [6] M. Chiew, N. N. Graedel, J. A. McNab, S. M. Smith, and K. L. Miller, “Accelerating functional mri using fixed-rank approximations and radial-cartesian sampling,” *Magnetic resonance in medicine*, vol. 76, no. 6, pp. 1825–1836, 2016.
- [7] Y. Tian, K. C. Erb, G. Adluru, D. Likhite, A. Pedgaonkar, M. Blatt, S. Kamesh Iyer, J. Roberts, and E. DiBella, “Evaluation of pre-reconstruction interpolation methods for iterative reconstruction of radial k-space data,” *Medical physics*, vol. 44, no. 8, pp. 4025–4034, 2017.
- [8] T. Benkert, Y. Tian, C. Huang, E. V. DiBella, H. Chandarana, and L. Feng, “Optimization and validation of accelerated golden-angle radial sparse mri reconstruction with self-calibrating grappa operator gridding,” *Magnetic Resonance in Medicine*, vol. 80, no. 1, pp. 286–293, 2018.
- [9] L. Feng, C. Huang, K. Shanbhogue, D. K. Sodickson, H. Chandarana, and R. Otazo, “Racer-grasp: respiratory-weighted, aortic contrast enhancement-guided and coil-unstreaking golden-angle radial sparse mri,” *Magnetic resonance in medicine*, vol. 80, no. 1, pp. 77–89, 2018.
- [10] S. Nayer and N. Vaswani, “Fast low rank column-wise compressive sensing,” *arXiv:2102.10217*.
- [11] S. Nayer, P. Narayanamurthy, and N. Vaswani, “Phaseless PCA: Low-rank matrix recovery from column-wise phaseless measurements,” in *Intl. Conf. Machine Learning (ICML)*, 2019.
- [12] S. Nayer and N. Vaswani, “Sample-efficient low rank phase retrieval,” *IEEE Trans. Info. Th.*, 2021.

- [13] R. S. Srinivasa, K. Lee, M. Junge, and J. Romberg, "Decentralized sketching of low rank matrices," in *Neur. Info. Proc. Sys. (NeurIPS)*, 2019, pp. 10 101–10 110.
- [14] L. Feng, L. Axel, H. Chandarana, K. T. Block, D. K. Sodickson, and R. Otazo, "Xd-grasp: golden-angle radial mri with reconstruction of extra motion-state dimensions using compressed sensing," *Magnetic resonance in medicine*, vol. 75, no. 2, pp. 775–788, 2016.
- [15] A. S. Gupta and Z. Liang, "Dynamic imaging by temporal modeling with principal component analysis," 2001, p. 10.
- [16] H. Pedersen, S. Kozerke, S. Ringgaard, K. Nehrke, and W. Y. Kim, "k-t pca: Temporally constrained k-t blast reconstruction using principal component analysis," *Magnetic resonance in medicine*, vol. 62, no. 3, pp. 706–716, 2009.
- [17] B. Zhao, J. P. Haldar, A. G. Christodoulou, and Z.-P. Liang, "Image reconstruction from highly undersampled-space data with joint partial separability and sparsity constraints," *Medical Imaging, IEEE Transactions on*, vol. 31, no. 9, pp. 1809–1820, 2012.
- [18] A. G. Christodoulou, T. K. Hitchens, Y. L. Wu, C. Ho, and Z.-P. Liang, "Improved subspace estimation for low-rank model-based accelerated cardiac imaging," *IEEE Transactions on Biomedical Engineering*, vol. 61, no. 9, pp. 2451–2457, 2014.
- [19] L. Feng, Q. Wen, C. Huang, A. Tong, F. Liu, and H. Chandarana, "Grasp-pro: improving grasp dce-mri through self-calibrating subspace-modeling and contrast phase automation," *Magnetic resonance in medicine*, vol. 83, no. 1, pp. 94–108, 2020.
- [20] E. J. Candès, X. Li, Y. Ma, and J. Wright, "Robust principal component analysis?" *J. ACM*, vol. 58, no. 3, 2011.
- [21] R. Otazo, E. Candès, and D. K. Sodickson, "Low-rank plus sparse matrix decomposition for accelerated dynamic mri with separation of background and dynamic components," *Magnetic resonance in medicine*, vol. 73, no. 3, pp. 1125–1136, 2015.
- [22] C. Y. Lin and J. A. Fessler, "Efficient dynamic parallel mri reconstruction for the low-rank plus sparse model," *IEEE transactions on computational imaging*, vol. 5, no. 1, pp. 17–26, 2018.
- [23] Y. Liu, T. Liu, J. Liu, and C. Zhu, "Smooth robust tensor principal component analysis for compressed sensing of dynamic mri," *Pattern Recognition*, vol. 102, p. 107252, 2020.
- [24] S. G. Lingala, E. DiBella, and M. Jacob, "Deformation corrected compressed sensing (dc-cs): a novel framework for accelerated dynamic mri," *IEEE transactions on medical imaging*, vol. 34, no. 1, pp. 72–85, 2014.
- [25] X. Chen, M. Salerno, Y. Yang, and F. H. Epstein, "Motion-compensated compressed sensing for dynamic contrast-enhanced mri using regional spatiotemporal sparsity and region tracking: Block low-rank sparsity with motion-guidance (blossm)," *Magnetic resonance in medicine*, vol. 72, no. 4, pp. 1028–1038, 2014.
- [26] A. Tolouee, J. Alirezaie, and P. Babyn, "Nonrigid motion compensation in compressed sensing reconstruction of cardiac cine mri," *Magnetic resonance imaging*, vol. 46, pp. 114–120, 2018.
- [27] Z. Ke, W. Huang, Z.-X. Cui, J. Cheng, S. Jia, H. Wang, X. Liu, H. Zheng, L. Ying, Y. Zhu, and D. Liang, "Learned low-rank priors in dynamic mr imaging," *IEEE Transactions on Medical Imaging*, vol. 40, no. 12, pp. 3698–3710, 2021.
- [28] A. H. Ahmed, H. Aggarwal, P. Nagpal, and M. Jacob, "Dynamic mri using deep manifold self-learning," in *IEEE 17th International Symposium on Biomedical Imaging (ISBI)*, 2020, pp. 1052–1055.
- [29] H. K. Aggarwal, M. P. Mani, and M. Jacob, "Modl: Model-based deep learning architecture for inverse problems," *IEEE transactions on medical imaging*, vol. 38, no. 2, pp. 394–405, 2018.
- [30] M. Arvinte, S. Vishwanath, A. H. Tewfik, and J. I. Tamir, "Deep j-sense: Accelerated mri reconstruction via unrolled alternating optimization," in *International Conference on Medical Image Computing and Computer-Assisted Intervention*. Springer, 2021, pp. 350–360.
- [31] J. Herrmann, G. Koerzdoerfer, D. Nickel, M. Mostapha, M. Nadar, S. Gassenmaier, T. Kuestner, and A. E. Othman, "Feasibility and implementation of a deep learning mr reconstruction for tse sequences in musculoskeletal imaging," *Diagnostics*, vol. 11, no. 8, p. 1484, 2021.
- [32] C. M. Sandino, P. Lai, S. S. Vasanawala, and J. Y. Cheng, "Accelerating cardiac cine mri using a deep learning-based espirit reconstruction," *Magnetic Resonance in Medicine*, vol. 85, no. 1, pp. 152–167, 2021.
- [33] E. J. Zucker, C. M. Sandino, A. Kino, P. Lai, and S. S. Vasanawala, "Free-breathing accelerated cardiac mri using deep learning: Validation in children and young adults," *Radiology*, vol. 300, no. 3, pp. 539–548, 2021.
- [34] V. Ghodrati, M. Bydder, A. Bedayat, A. Prosper, T. Yoshida, K.-L. Nguyen, J. P. Finn, and P. Hu, "Temporally aware volumetric generative adversarial network-based mr image reconstruction with simultaneous respiratory motion compensation: Initial feasibility in 3d dynamic cine cardiac mri," *Magnetic Resonance in Medicine*, vol. 86, no. 5, pp. 2666–2683, 2021.
- [35] T. Küstner, N. Fuin, K. Hammernik, A. Bustin, H. Qi, R. Hajhosseiny, P. G. Masci, R. Neji, D. Rueckert, R. M. Botnar, *et al.*, "Cinenet: deep learning-based 3d cardiac cine mri reconstruction with multi-coil complex-valued 4d spatio-temporal convolutions," *Scientific reports*, vol. 10, no. 1, pp. 1–13, 2020.
- [36] A. H. Ahmed, Q. Zou, P. Nagpal, and M. Jacob, "Dynamic imaging using deep bi-linear unsupervised representation (deblur)," *IEEE transactions on medical imaging*, 2022.
- [37] E. K. Cole, F. Ong, S. S. Vasanawala, and J. M. Pauly, "Fast unsupervised mri reconstruction without fully-sampled ground truth data using generative adversarial networks," in *Proceedings of the IEEE/CVF International Conference on Computer Vision*, 2021, pp. 3988–3997.
- [38] S. Ravishankar, B. E. Moore, R. R. Nadakuditi, and J. A. Fessler, "Low-rank and adaptive sparse signal (lassi) models for highly accelerated dynamic imaging," *IEEE transactions on medical imaging*, vol. 36, no. 5, pp. 1116–1128, 2017.
- [39] B. E. Moore, S. Ravishankar, R. R. Nadakuditi, and J. A. Fessler, "Online adaptive image reconstruction (onair) using dictionary models," *IEEE transactions on computational imaging*, vol. 6, pp. 153–166, 2019.
- [40] E. J. Candès and B. Recht, "Exact matrix completion via convex optimization," *Found. of Comput. Math*, no. 9, pp. 717–772, 2008.
- [41] Y. Cherapanamjeri, K. Gupta, and P. Jain, "Nearly-optimal robust matrix completion," *ICML*, 2016.
- [42] X. Yi, D. Park, Y. Chen, and C. Caramanis, "Fast algorithms for robust pca via gradient descent," in *Neur. Info. Proc. Sys. (NeurIPS)*, 2016.
- [43] Q. Zheng and J. Lafferty, "Convergence analysis for rectangular matrix completion using burer-monteiro factorization and gradient descent," *arXiv preprint arXiv:1605.07051*, 2016.
- [44] "Stanford cgls code," <https://web.stanford.edu/group/SOL/software/cgls/>.
- [45] P. Netrapalli, P. Jain, and S. Sanghavi, "Low-rank matrix completion using alternating minimization," in *Annual ACM Symp. on Th. of Comp. (STOC)*, 2013.
- [46] J.-L. Starck, D. L. Donoho, and E. J. Candès, "Astronomical image representation by the curvelet transform," *Astronomy & Astrophysics*, vol. 398, no. 2, pp. 785–800, 2003.
- [47] C. Chen, Y. Liu, P. Schniter, M. Tong, K. Zareba, O. Simonetti, L. Potter, and R. Ahmad, "Ocmr (v1. 0)–open-access multi-coil k-space dataset for cardiovascular magnetic resonance imaging," *arXiv preprint arXiv:2008.03410*, 2020.
- [48] S. Winkelmann, T. Schaeffter, T. Koehler, H. Eggers, and O. Doessel, "An optimal radial profile order based on the golden ratio for time-resolved mri," *IEEE transactions on medical imaging*, vol. 26, no. 1, pp. 68–76, 2006.
- [49] J. A. Fessler and B. P. Sutton, "Nonuniform fast fourier transforms using min-max interpolation," *IEEE Transactions on Signal Processing*, vol. 51, no. 2, pp. 560–574, 2003.
- [50] D. O. Walsh, A. F. Gmitro, and M. W. Marcellin, "Adaptive reconstruction of phased array MR imagery," *Magnetic Resonance in Medicine*, vol. 43, no. 5, pp. 682–690, 2000.

	altGDmin [aGm-2]	altGDmin w/ Mean	AltMin	Mixed-norm
Gauss.	0.0104 (0.15) [0.0077 (0.29)]	0.0090 (0.18)	0.1126 (12.73)	0.0291 (41.80)
Four.	0.3309(0.50)	0.0016 (0.55)	0.0249 (85.82)	1 (145.50)

TABLE V: Comparison with two approaches from theoretical literature on a 30 x 30 piece of the PINCAT Sequence ($n = 900, q = 50$) using $m = n/10$ random Gaussian (Gaussian) or Fourier (Four.) measurements. aGm-2 is altGDmin with $\epsilon_{exit} = 0.001$. We report **Error (Time in seconds)**. Here Error is the Monte Carlo average of $\|\hat{\mathbf{X}} - \mathbf{X}^*\|_F^2 / \|\mathbf{X}^*\|_F^2$ over 50 realizations.

APPENDIX A

COMPARISON WITH PROVABLY CORRECT ALGORITHMS FOR LRCCS

We compared altGDmin-basic with two other algorithms that also come with provable guarantees: the solver for mixed norm minimization studied in [13] and the AltMin algorithm studied in [11], [12], modified for the linear LRCCS problem (replace the PR step for updating \mathbf{b}_k 's by a simple LS step). In both cases we used author code downloaded from https://www.dropbox.com/sh/lywtzc0y9awpvgz/AABjuiuLWPy_8y7C3GQKo8pa?dl=0 (for mixed norm min) and <https://github.com/praneethmurthy/> (for AltMin).

Since these algorithms were designed and evaluated only for random Gaussian measurements, their code cannot be easily modified to handle large-sized image sequences or complicated MRI sampling patterns. Hence, for this experiment, we use a 30 x 30 size piece of the PINCAT image sequence with 50 frames and simulate (i) random Gaussian \mathbf{A}_k 's and (ii) random Fourier \mathbf{A}_k 's. Thus $n = 30^2 = 900$, and $q = 50$. For (ii), the sampling mask is obtained by selecting m 2D-DFT frequency ‘‘locations’’ uniformly at random from all n possible ones. We report the results in Table V for $m = n/10$ in both cases. We provide results for two versions of altGDmin (Algorithm 1) and altGDmin-0.0001 (this is Algorithm 1 with the exit threshold $\epsilon_{exit} = 0.001$ instead of 0.01). As can be seen, for both random Gaussian and random Fourier measurements, altGDmin and altGDmin has lower reconstruction error than the other two, while also being much faster.

In the random Fourier setting, since we are selecting random frequencies, if enough lower frequencies are not selected, the reconstruction error can be large. If the mean image is computed and subtracted, the energy in the lower spatial frequencies is a lot lower. This is why use of mean subtraction (altGDmin-mean) significantly reduces the error in this case.

APPENDIX B GUARANTEES

In [10], we studied the basic LRCCS problem and algorithm. We showed the following in [10]:

Theorem 2.1. Assume that the matrices \mathbf{A}_k are i.i.d. $m_k \times n$ matrices with each having i.i.d. Gaussian entries and that \mathbf{X}^* is a rank r matrix that satisfies Assumption 2.1. Consider Algorithm 1 with the following changes: (i) Set parameters as $\eta = 0.5/\sigma_{\max}^*$, $\tilde{C} = 6\kappa^2\mu^2$, $\hat{r} = r$, $T = C\kappa^2 \log(1/\epsilon)$, and remove the exit loop step (line 17). (ii) Assume sample-splitting, i.e., a new independent set of $m/(2T + 1)$ samples

is used in the initialization, and also in each update step for $\hat{\mathbf{U}}$ and $\hat{\mathbf{B}}$. Then, if

$$mq \geq C\kappa^6\mu^2(n+q)r^2 \log(1/\epsilon), \quad m \geq C \max(\log q, \log n),$$

then, with probability at least $1 - n^{-10}$,

$$\|\mathbf{x}_k^* - \hat{\mathbf{x}}_k\| \leq \epsilon \|\mathbf{x}_k^*\| \quad \text{and} \quad \|\mathbf{X}^* - \hat{\mathbf{X}}\|_F \leq \epsilon \|\mathbf{X}^*\|.$$

The time complexity is $O(\kappa^2 m q n r \log(1/\epsilon))$.

Consider the time-varying measurements’ setting. For doing this, define

$$\bar{m} = \sum_k m_k/q, \quad m_{\min} = \min_k m_k, \quad m_{\max} = \max_k m_k$$

In this case, we can prove the following corollary

Corollary 2.2. In the setting of Theorem 2.1, if $\eta = \frac{0.5\bar{m}}{\sigma_{\max}^* m_{\max}^2}$, $\tilde{C} = 9\kappa^2\mu^2 \frac{m_{\max}^2}{m_{\min}^2}$, and if $\bar{m}q \geq C\kappa^6\mu^2 \frac{m_{\max}^4}{m_{\min}^4} (n+q)r^2 \log(1/\epsilon)$, and $m_{\min} \geq C \max(\log q, \log n)$, then, with probability at least $1 - n^{-10}$, $\|\mathbf{x}_k^* - \hat{\mathbf{x}}_k\| \leq \epsilon \|\mathbf{x}_k^*\|$ and $\|\mathbf{X}^* - \hat{\mathbf{X}}\|_F \leq \epsilon \|\mathbf{X}^*\|$.

Notice that the only change is the extra factor of $(m_{\max}/m_{\min})^4$ in the sample complexity and similar changes to η, \tilde{C} . If all m_k s are quite similar, this does not change the result much. In case of both radial and golden-angle sampling (the two commonly used schemes), this is true. For example for the brain sequence and 16 radial lines, $m_{\max}/m_{\min} = 1.02$.

Proof outline: The proof follows using the exact same approach as that in [10] once we can consider the matrix $\mathbf{X}^*_w = \mathbf{X}^* \mathbf{D}_w$ with $\mathbf{D}_w = \text{diag}(\sqrt{m_k/\bar{m}}, k \in [q])$ being a diagonal $q \times q$ matrix with diagonal entries $\sqrt{m_k/\bar{m}}$. With this change, it is possible to prove the same result as in our earlier work, but with κ, μ replaced by κ_w, μ_w for the matrix \mathbf{X}^*_w . Furthermore, it is easy to show that $\kappa_w \leq \kappa \sqrt{m_{\max}/m_{\min}}$ and $\mu_w \leq \mu \sqrt{m_{\max}/m_{\min}}$. Thus, $\kappa_w^6 \mu_w^2 \leq \kappa^6 \mu^2 (m_{\max}/m_{\min})^4$ and this is what introduces the extra factor of $(m_{\max}/m_{\min})^4$ in our sample complexity.

The complete proof and discussion for the time-varying m_k setting will be part of a forthcoming short paper.

APPENDIX C

DATASET DETAILS FOR RETROSPECTIVELY UNDERSAMPLED EXPERIMENTS

Fully sampled multi coil datasets acquired on a Cartesian grid in different dynamic MRI applications were retrospectively downsampled using a 1D Cartesian undersampling mask, or a 2D pseudo radial sampling mask. Details are provided below:

- 1) A breath held cardiac perfusion dataset with dimensions $k_x \times k_y \times n_t \times n_c = 128 \times 128 \times 40 \times 12$ previously used in [21], [22].
- 2) A breath held cardiac cine dataset with dimensions of $k_x \times k_y \times n_t \times n_c = 256 \times 256 \times 24 \times 12$ previously used in [21], [22].
- 3) A low spatial but high temporal resolution speech data set with dimensions of $k_x \times k_y \times n_t \times n_c = 68 \times 68 \times 2048 \times 16$. This data was acquired at the University of Iowa on a healthy volunteer producing a variety of

speech sounds including uttering interleaved vowel and consonant sounds (za-na-za-loo-lee-laa), and counting numbers at the subjects natural speaking rate. Since the subject was speaking at the natural rate, the spatial resolution was compromised to $3.4 \times 3.4 \text{mm}^2$ and the temporal resolution was maintained at 70 ms/frame to capture the motion of the articulators.

- 4) A brain multi-parameter (T2, and T1-rho) mapping dataset with dimensions of $k_x \times k_y \times n_t \times n_c = 128 \times 128 \times 24 \times 12$ previously used in [21], [22]. This was acquired on a normal volunteer at the University of Iowa. Spin lock times and echo times were varied to estimate T2, and T1-rho (T1 in rotating frame) time constants from the resulting multi-contrast (or loosely dynamic) image frames.
- 5) Two representative breath held short axis cardiac cine datasets from the OCMR database [47] with dimensions respectively $k_x \times k_y \times n_t \times n_c = 192 \times 144 \times 25 \times 38$; and $k_x \times k_y \times n_t \times n_c = 192 \times 150 \times 15 \times 30$.
- 6) One free breathing ungated cardiac perfusion dataset, previously used in [24] with dimensions $k_x \times k_y \times n_t \times n_c = 288 \times 108 \times 200 \times 32$. This dataset had both perfusion dynamics and motion dynamics due to cardiac and breathing motion. The dataset was acquired at the University of Utah with TR/TE=2.5/1ms; saturation recovery time=100 ms.
- 7) PINCAT: Free breathing PINCAT perfusion phantom containing dynamics due to perfusion uptake in the heart as well as heavy breathing motion. This phantom was previously used in the works of [4], [22].

For multi coil experiments, the raw data of datasets in (3)-(6) above were coil compressed into 8 virtual coils. The virtual coil sensitivity maps were estimated using the Walsh eigen decomposition algorithm [50] from time averaged undersampled data. For datasets in (1), and (2), we did not perform any coil compression, and used the author provided coil sensitivity maps.

Data sets in (1) and (2) above were undersampled using 1D variable density random undersampling mask at reduction factors (R); R=8, R=6 respectively.

Data sets in (3),(4),(5),(6),(7) above were undersampled using 2D pseudo radial undersampling with golden angle interleaving between spokes at different reduction factors using 16, 8, and 4 radial lines.

Finally, single coil experiments were performed on datasets (3)-(7). Except for the PINCAT phantom, to simulate single coil from the multi coil data, we first coil combined the original fully sampled data using the estimated coil maps, and then retrospectively undersampled using pseudo radial mask with 16,8,4 radial lines.

APPENDIX D

EXPERIMENTS ON PROSPECTIVELY UNDER-SAMPLED RADIAL DATA

To demonstrate applicability of our algorithm on prospectively under-sampled data, we considered reconstructing two open source prospectively under-sampled radial datasets.

The first dataset was a free breathing un-gated cardiac perfusion dataset previously used in [7], which had both cardiac, breathing motions along with contrast uptake dynamics. The open source provided raw k-space dataset dimensions were 288 read out points, 24 radial spokes with golden angle based angular increments, 133 time frames, and 7 virtual coils after PCA based coil compression.

The second dataset was an abdomen dynamic contrast enhanced (DCE-MRI) dataset previously used in [21], and had contrast uptake dynamics predominantly with minimal motion. The raw dataset dimensions were 384 read out points, 21 radial spokes with golden angle based angular increments, 28 time frames, and 12 coils.

Similar to several previous studies [7], [8], [9], we first pre interpolated the radial data onto a Cartesian grid by using the GROG operator pregridding, and then passed the resulting raw data to our reconstruction algorithm. We also qualitatively compared the above against our algorithm which has an implementation of iNUFFT and NUFFT in the forward and backward model and operates directly on true radial data.

Since there is no ground truth, we finally show qualitative reconstructions with individual spatial frames and time series and compare against the direct inverse NUFFT reconstruction, and author provided reconstructions in the above open source datasets. The reconstructions were a spatio temporal total variation constrained reconstruction operated on GROG gridded data in ungated cardiac perfusion dataset, and LplusS-Lin reconstruction operated on true radial data in the abdomen DCE dataset.

A. Results

In figure (4), we qualitative observe that the proposed altDGmin2 reconstruction depict the cardiac, breathing motions, and also the contrast uptake dynamics in the heart reasonably well, while resolving undersampling streak artifacts present in the direct iNUFFT reconstructions. In figure (5), we observe the contrast uptake dynamics through the liver and other blood vessels are well resolved, but slight residual alias artifacts remain in altgdm2.

Since there is no ground truth available in prospective undersampling experiments, we did not performed detailed qualitative comparisons against existing reconstruction algorithms. A detailed comparison against existing state of art reconstruction algorithms will need blinded image quality rating from radiologists considering application specific criterion. This is beyond the scope of this paper, and will be a scope for a future study.

APPENDIX E

COMPARING L+S-LIN [22] FOR TWO PARAMETER VALUE CHOICES FOR SINGLE-COIL DATA

In Table VI, we report results for L+S-Lin using two parameter choices: parameters for cardiac used for all experiments and parameters for PINCAT used for all experiments. As can be seen the former results in significantly lower recovery errors and is faster. Hence for all other experiments we only used L+S-Lin with cardiac parameters.

Dataset(Radial)	L+S-ktslr	L+S-Otazo	L+S-Lin cardiac params PINCAT params	altGDmin-mean	altGDmin-MRI	altGDmin-MRI2
brain-T2-T1(4)	0.0676 (15.52)	0.0210 (3.61)	0.0875 (1.04) 0.0810	0.0221 (0.55)	0.0212 (0.51)	0.0212 (0.58)
brain-T2-T1(8)	0.0227 (14.60)	0.0101 (1.99)	0.0151 (1.02) 0.0116	0.0114 (0.53)	0.0101 (0.57)	0.0101 (0.55)
brain-T2-T1(16)	0.0094 (12.82)	0.0046 (1.37)	0.0046 (0.94) 0.0048	0.0070 (0.52)	0.0052 (0.55)	0.0052 (0.57)
Cardiac-ocmr-data(4)	0.1425 (29.32)	0.0818 (6.76)	0.1731 (1.82) 0.2964	0.0253 (3.27)	0.0249 (2.60)	0.0252 (3.47)
Cardiac-ocmr-data(8)	0.0704 (28.76)	0.0232 (6.70)	0.0965 (1.85) 0.1707	0.0104 (3.37)	0.0102 (2.59)	0.0102 (3.52)
Cardiac-ocmr-data(16)	0.0100 (29.03)	0.0063 (5.23)	0.0236 (1.82) 0.0511	0.0060 (2.23)	0.0057 (2.41)	0.0057 (2.48)
speech-seq(4)	0.1876 (24.25)	0.2229 (6.16)	0.1947 (1.70) 0.4729	0.2027 (2.74)	0.1836 (2.17)	0.1939 (2.88)
speech-seq(8)	0.0936 (23.57)	0.0764 (6.20)	0.0914 (1.68) 0.1934	0.1290 (1.45)	0.1133 (1.61)	0.1131 (1.63)
speech-seq(16)	0.0470 (17.15)	0.0414 (4.50)	0.0441 (1.65) 0.0673	0.1024 (1.10)	0.0713 (1.19)	0.0711 (1.21)
FB-ungated(4)	0.3854 (108.96)	0.3400 (25.71)	0.4569 (7.29) 0.5614	0.2408 (7.27)	0.2383 (7.68)	0.2382 (8.05)
FB-ungated(8)	0.2507 (109.19)	0.1721 (25.53)	0.2981 (7.33) 0.3358	0.1604 (5.95)	0.1499 (6.16)	0.1497 (6.55)
FB-ungated(16)	0.1539 (107.67)	0.1058 (24.02)	0.1568 (7.31) 0.1536	0.1391 (3.93)	0.1177 (4.33)	0.1174 (4.56)
lowres-speech(4)	0.2418 (261.76)	0.2496 (733.64)	0.4171 (360.95) 0.2974	0.1758 (42.23)	0.1704 (33.31)	0.1679 (44.82)
lowres-speech(8)	0.1758 (523.70)	0.1770 (722.61)	0.2395 (356.00) 0.1591	0.1382 (59.98)	0.1224 (45.77)	0.1208 (62.10)
lowres-speech(16)	0.1183 (182.14)	0.1277 (632.37)	0.1331 (362.05) 0.1160	0.1249 (45.08)	0.0952 (43.81)	0.0952 (44.51)
Pincat(4)	0.0445 (34.85)	0.0381 (8.04)	0.1054 (2.26) 0.0766	0.0294 (1.51)	0.0278 (1.63)	0.0278 (1.77)
Pincat(8)	0.0216 (31.54)	0.0162 (3.91)	0.0208 (2.22) 0.0148	0.0197 (1.21)	0.0166 (1.36)	0.0166 (1.31)
Pincat(16)	0.0095 (23.31)	0.0065 (2.70)	0.0047 (2.25) 0.0063	0.0162 (1.10)	0.0097 (1.08)	0.0097 (1.13)
average-Error (avg-time)	0.1140 (87.67)	0.0956 (123.39)	0.1424 (62.28) 0.1706	0.0867 (10.22)	0.0774 (8.85)	0.0777 (10.64)

TABLE VI: Single-coil comparisons: Comparing *ktSLR* [4], *L+S-Otazo* [21], *L+S-Lin* [22], *altGDmin* [10], *altGDmin-MRI* and *altGDmin-MRI2* and the Deep Learning (DL) algorithm of [29], for 6 very different dynamic MRI sequences and 3 choices of undersampling factors. For *ktSLR* and *L+S-Otazo* we used the parameters for cardiac. For *L+S-Lin* we report two results in two rows. The first row used parameters for cardiac, the second used parameters for PINCAT (both were provided by authors). The last row shows the average-Error (total-Time), with average taken over all 18 previous results. Dataset sizes: PINCAT ($n = 16384, 50$), Brain ($n = 16384, q = 24$), Vocal tract ($n = 10000, q = 59$), Cardiac-cine ($n = 27648, q = 25$), lowres-speech ($n = 3600, q = 2048$), cardiac-free-breathing (cardiac-fb) ($n = 31104, q = 80$).

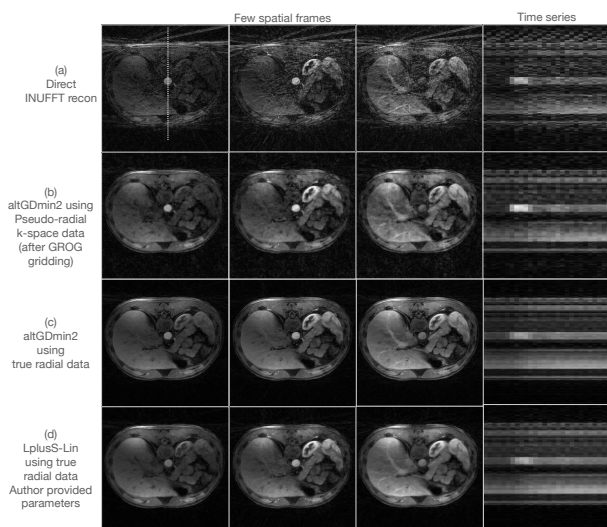


Fig. 4: Visual image quality comparison-prospective data 1

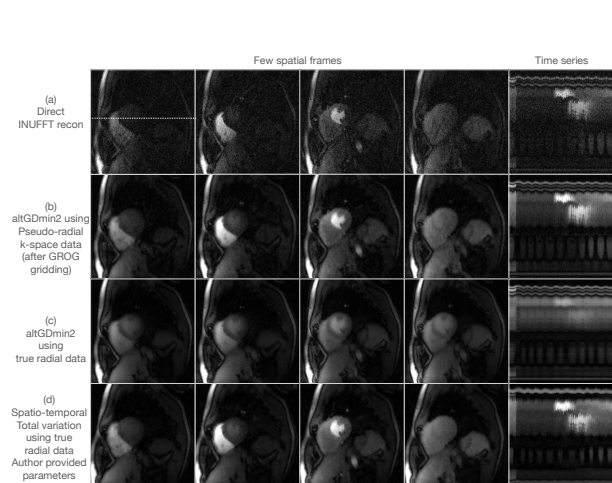


Fig. 5: Visual image quality comparison-prospective data 2